59

SATELLITE & MESOMETEOROLOGY RESEARCH PROJECT

Department of the Geophysical Sciences
The University of Chicago

USE OF WET-BEAM DOPPLER WINDS IN THE DETERMINATION OF THE VERTICAL VELOCITY OF RAINDROPS INSIDE HURRICANE RAINBANDS

by

Tetsuya Fujita, Peter G. Black, and Arthur G. Loesch

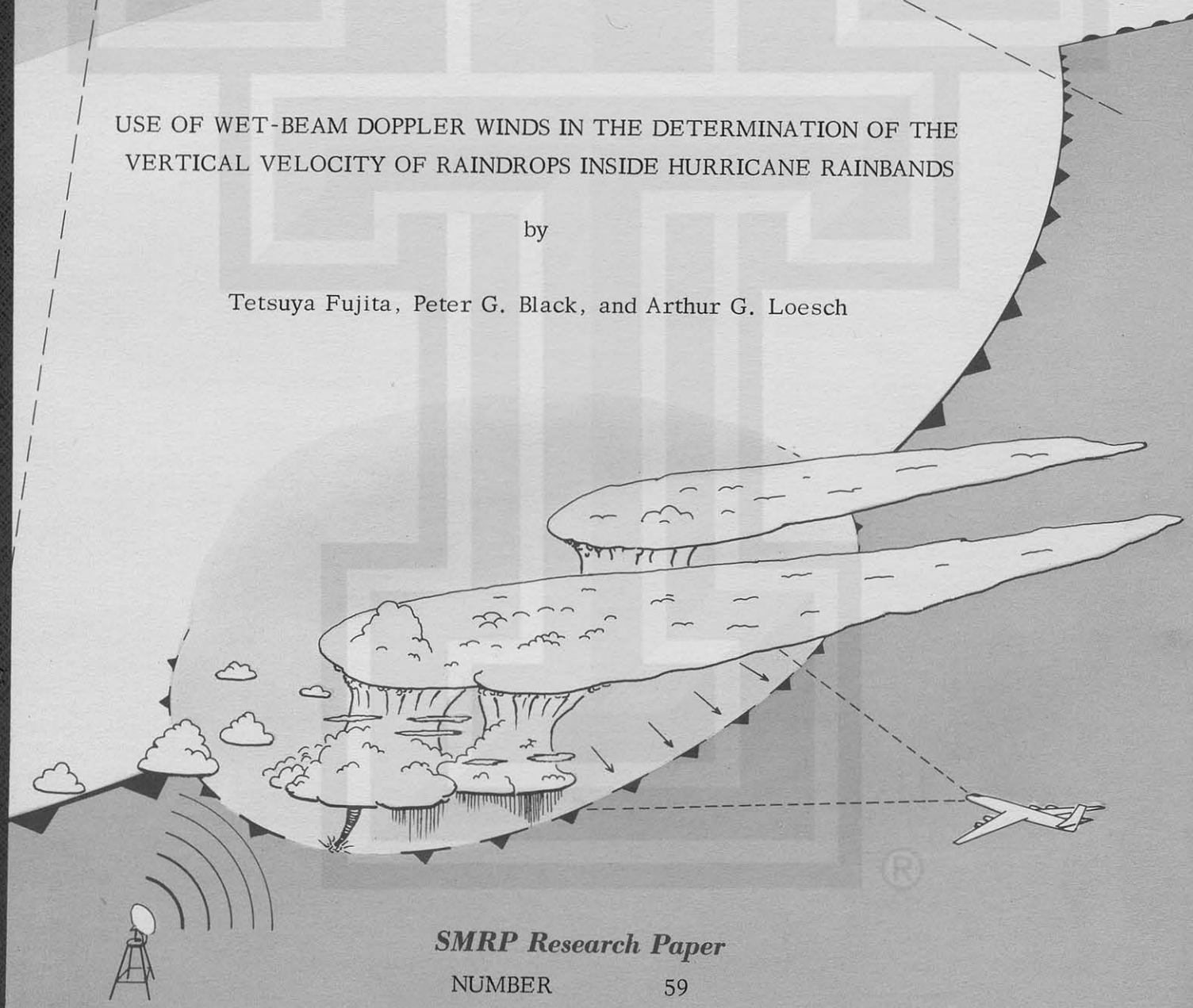

SMRP Research Paper

NUMBER 59

April 1966

MESOMETEOROLOGY PROJECT --- RESEARCH PAPERS

1.* Report on the Chicago Tornado of March 4, 1961 - Rodger A. Brown and Tetsuya Fujita

2.* Index to the NSSP Surface Network - Tetsuya Fujita

3.* Outline of a Technique for Precise Rectification of Satellite Cloud Photographs - Tetsuya Fujita

4.* Horizontal Structure of Mountain Winds - Henry A. Brown

5.* An Investigation of Developmental Processes of the Wake Depression Through Excess Pressure Analysis of Nocturnal Showers - Joseph L. Goldman

6.* Precipitation in the 1960 Flagstaff Mesometeorological Network - Kenneth A. Styber

7.** On a Method of Single- and Dual-Image Photogrammetry of Panoramic Aerial Photographs - Tetsuya Fujita

8. A Review of Researches on Analytical Mesometeorology - Tetsuya Fujita

9. Meteorological Interpretations of Convective Nephsystems Appearing in TIROS Cloud Photographs - Tetsuya Fujita, Toshimitsu Ushijima, William A. Hass, and George T. Dellert, Jr.

10. Study of the Development of Prefrontal Squall-Systems Using NSSP Network Data - Joseph L. Goldman

11. Analysis of Selected Aircraft Data from NSSP Operation, 1962 - Tetsuya Fujita

12. Study of a Long Condensation Trail Photographed by TIROS I - Toshimitsu Ushijima

13. A Technique for Precise Analysis of Satellite Data; Volume I - Photogrammetry (Published as MSL Report No. 14) - Tetsuya Fujita

14. Investigation of a Summer Jet Stream Using TIROS and Aerological Data - Kozo Ninomiya

15. Outline of a Theory and Examples for Precise Analysis of Satellite Radiation Data - Tetsuya Fujita

16. Preliminary Result of Analysis of the Cumulonimbus Cloud of April 21, 1961 - Tetsuya Fujita and James Arnold

17. A Technique for Precise Analysis of Satellite Photographs - Tetsuya Fujita

18. Evaluation of Limb Darkening from TIROS III Radiation Data - S.H.H. Larsen, Tetsuya Fujita, and W.L. Fletcher

19. Synoptic Interpretation of TIROS III Measurements of Infrared Radiation - Finn Pedersen and Tetsuya Fujita

20. TIROS III Measurements of Terrestrial Radiation and Reflected and Scattered Solar Radiation - S.H.H. Larsen, Tetsuya Fujita, and W.L. Fletcher

21. On the Low-level Structure of a Squall Line - Henry A. Brown

22. Thunderstorms and the Low-level Jet - William D. Bonner

23. The Mesoanalysis of an Organized Convective System - Henry A. Brown

24. Preliminary Radar and Photogrammetric Study of the Illinois Tornadoes of April 17 and 22, 1963 - Joseph L. Goldman and Tetsuya Fujita

25. Use of TIROS Pictures for Studies of the Internal Structure of Tropical Storms - Tetsuya Fujita with Rectified Pictures from TIROS I Orbit 125, R/O 128 - Toshimitsu Ushijima

26. An Experiment in the Determination of Geostrophic and Isallobaric Winds from NSSP Pressure Data - William Bonner

27. Proposed Mechanism of Hook Echo Formation - Tetsuya Fujita with a Preliminary Mesosynoptic Analysis of Tornado Cyclone Case of May 26, 1963 - Tetsuya Fujita and Robbi Stuhmer

28. The Decaying Stage of Hurricane Anna of July 1961 as Portrayed by TIROS Cloud Photographs and Infrared Radiation from the Top of the Storm - Tetsuya Fujita and James Arnold

29. A Technique for Precise Analysis of Satellite Data, Volume II - Radiation Analysis, Section 6. Fixed-Position Scanning - Tetsuya Fujita

30. Evaluation of Errors in the Graphical Rectification of Satellite Photographs - Tetsuya Fujita

31. Tables of Scan Nadir and Horizontal Angles - William D. Bonner

32. A Simplified Grid Technique for Determining Scan Lines Generated by the TIROS Scanning Radiometer - James E. Arnold

33. A Study of Cumulus Clouds over the Flagstaff Research Network with the Use of U-2 Photographs - Dorothy L. Bradbury and Tetsuya Fujita

34. The Scanning Printer and Its Application to Detailed Analysis of Satellite Radiation Data - Tetsuya Fujita

35. Synoptic Study of Cold Air Outbreak over the Mediterranean using Satellite Photographs and Radiation Data - Aasmund Rabbe and Tetsuya Fujita

36. Accurate Calibration of Doppler Winds for their use in the Computation of Mesoscale Wind Fields - Tetsuya Fujita

37. Proposed Operation of Intrumented Aircraft for Research on Moisture Fronts and Wake Depressions - Tetsuya Fujita and Dorothy L. Bradbury

38. Statistical and Kinematical Properties of the Low-level Jet Stream - William D. Bonner

39. The Illinois Tornadoes of 17 and 22 April 1963 - Joseph L. Goldman

40. Resolution of the Nimbus High Resolution Infrared Radiometer - Tetsuya Fujita and William R. Bandeen

41. On the Determination of the Exchange Coefficients in Convective Clouds - Rodger A. Brown

* Out of Print
** To be published

(Continued on back cover)

SATELLITE AND MESOMETEOROLOGY RESEARCH PROJECT
Department of the Geophysical Sciences
The University of Chicago

USE OF WET-BEAM DOPPLER WINDS IN THE DETERMINATION OF THE VERTICAL VELOCITY OF RAINDROPS INSIDE HURRICANE RAINBANDS

by

Tetsuya Fujita, Peter G. Black, and Arthur G. Loesch

SMRP Research Paper #59
April, 1966

This research has been sponsored by the National Hurricane Research Laboratory, Environmental Science Services Administration under Grant Cwb WBG-41.

USE OF WET-BEAM DOPPLER WINDS IN THE DETERMINATION OF THE VERTICAL VELOCITY OF RAINDROPS INSIDE HURRICANE RAINBANDS[1]

Tetsuya Fujita, Peter G. Black, and Arthur G. Loesch

Department of the Geophysical Sciences
The University of Chicago
Chicago, Illinois

ABSTRACT

In order to solve the problem of the zero Doppler winds that occur during traverses through intense hurricane rainbands, a complete examination of the processes of wind-velocity determination by an APN-82 Doppler wind system has been attempted. It was revealed that the measured frequency shifts depend not only upon the degree of beam attenuation due to the raindrops but also upon the modes of frequency-shift determination by the frequency tracker. The separation of the return signals from the ground and the precipitation determines the three tracking modes called linear, transient, and locking modes. The linear mode occurs only when the difference between the horizontal speed of the raindrops and the true air speed is less than about 20% of the latter. This mode is unlikely to occur during rainband traverses inside an intense hurricane. Both transient- and locking-mode tracking usually occurs in hurricanes, resulting in the determination of either ground or true air velocities by a Doppler system. Because the differential frequency shift determines the Doppler velocity, the Doppler winds can be determined with extreme accuracy when either front or rear beams lock onto the raindrops while the other beams keep measuring the frequency shift of the signal from the ground. Winds thus determined give a median-intensity wind which is not at all affected by the tracking mode. The solution of the equations involving the frequency shift due to both the horizontal and vertical velocity of the raindrops revealed that the vector difference between this median-intensity wind and half of the dry-beam wind is proportional to the vertical velocity of the raindrops attenuating two of the four beams. Taking advantage of these

---

[1]This research has been sponsored by the National Hurricane Research Laboratory, Environmental Science Services Administration under Grant Cwb WBG-41.

characteristics, vertical velocities ranging between ±15 m sec^{-1} were computed during traverses near the outer walls of the rainbands. A nearly uniform vertical velocity of +3 m sec^{-1} (downward) on the average was obtained near the inner walls of the rainbands.

1. Introduction.

Since 1958 when the AN/APN-82 system, which includes the four-beam Doppler radar and the ASN-6 analog computer, became available to the National Hurricane Research Laboratory, the winds measured by the system have been used by many hurricane researchers in determining hurricane circulation at various levels. The system, originally developed for navigational purposes, was modified prior to its installation on the instrumented DC-6 and B-57 aircraft in order to obtain a faster response time.

As long as the APN-82 winds are used in the study of hurricanes as a whole, their accuracies in both direction and speed are quite adequate. After the accumulation of several years' penetration data through hurricanes, a number of researchers began to use these winds for detailed analysis of wind fields associated with mesoscale convective systems such as hot towers, rainbands, and eye-wall circulation.

A pioneering work on the scales of motion within hurricanes was attempted by Gray (1965a. and 1965b.),who used APN-82 winds and other data at one- or two-second intervals. He found that the response of the APN-82 system is not fast enough to represent actual winds, especially when their variation is appreciable.

With the use of penetration data by RFF's DC-6Bs and B-57, Gentry (1964) made detailed analyses of wind, temperature, and D-value fields within mesoscale areas that include the rainbands of hurricanes Becky, Cleo, Daisy, and Helene of 1958 and Ella of 1962. One of the most important problems brought to attention was the influence of the moving sea surface, the sea spray, and the heavy concentration of water droplets on Doppler-wind measurements. He postulated that the signal from the fast-moving spray would be less than that of the relatively stationary water in the upper layer of the ocean and then proceeded to a discussion of the influence of raindrops on APN-82 winds.

Almost all penetration data collected through 1962 and analyzed by Gentry supported the manufacturer's statement that the Doppler beams lock onto the strongest return signal, thus permitting the aircraft to measure the ground velocity with respect

to either the land or ocean surface. Gentry predicted, however, that the Doppler would measure the "zero wind" if it were taking the return signals from the raindrops near the aircraft, because it is likely that they move with the wind.

One year later, on October 3, 1963, one of RFF's DC-6Bs measured eight cases of zero or near-zero winds while flying repeatedly through rainbands near the eye wall of Hurricane Flora, which was then about 100 miles to the south of Hispaniola. It was this new evidence that stimulated the authors' interest in the extent to which the high concentration of raindrops attenuates Doppler beams completely before reaching the ground or sea surface.

2. Zero Doppler winds measured inside Hurricane Flora of 1963.

When RFF's DC-6B made a series of normal traverses at about 10,000 ft through the eye of Flora on October 3, 1963, the measured Doppler winds dropped to practically zero. There have been no known cases involving such a pronounced and extensive drop in the wind speed near the center of a rainband.

Figure 1 shows a schematic distribution of the rainbands and the true aircraft track along which the zero winds were measured at about 1612 and 1623 GMT when the aircraft was flying near the center of the rainbands. During the traverse period, 1310 to 1710 GMT, the storm's center was moving northwest at about 9 kt, and the maximum winds around the eye wall were as high as 120 kt. Practically all PPI pictures taken during the traverse include ground echoes of the mountains, as shown in the figure, thus permitting us to determine the exact locations of the aircraft as well as of the rainbands.

The radial distribution of the winds measured during seven passes made successively along the orientation ESE-WNW through the eye is summarized in Fig. 2. The altitude of the aircraft was about 10,000 ft during the entire period of four hours. At the end of each pass, a sharp U-turn was made in order to complete a large number of normal traverses through the storm center. In order to distinguish winds measured inside and outside the rainbands, the times when the aircraft was flying through significant rainbands appearing on the PPI photographs were determined and entered as vertical lines below each wind-speed curve. The areas of the winds measured outside these rainbands are stippled.

Fifteen rainband traverses, presumably affected by the Doppler wet beams as defined by Fujita (1966), are identified by letters A through O, of which nine are characterized by "near zero winds." It should be noted that the majority of the

wet-beam effects is seen inside the eye-wall rainband, but another rainband about 30 nm to the southeast also showed occasional but significant zero winds.

3. Definition of Individual, Weighted, and ASN Winds.

The antenna of the four-beam Doppler system, both pitch and roll stabilized, is designed to rotate around a vertical axis until the differential frequency shifts of a pair of opposite beams become identical. The nadir angle of the beam is, therefore, maintained constant, $\eta_0 = 30.50°$. A vector, called the Doppler heading, bisects the horizontal angle between two front beams. The horizontal angle between the Doppler heading and the front beams is $\psi_0 = 42.43°$. Two pairs of opposite beams are fired alternately at 0.5-sec intervals, thus allowing a comparison of differential frequency shifts at one-second intervals. The antenna is then rotated through a nulling process until the differential frequency shifts from the two pairs of beams become identical.

After obtaining the drift angles and the ground speed at one-second intervals, the system computes the wind directions and speeds directly from these values, using the instantaneous values of true air speeds and true headings. The raw winds thus computed are called in this paper the "individual winds" and are expressed by W, the speed, and w, the direction.

In view of the fluctuation of the true air velocity and of a certain time lag in the antenna rotation, the modified APN-82 and ASN-6 systems on board RFF's DC-6Bs and B-57 computes averaged winds after applying a weighting function.

$$F(t_0 - t) = e^{-B(t_0 - t)} \qquad (1)$$

where t_0 is the time of wind computation and B, a constant which is selected in order to decrease the weighting function to 0.05 at the maximum time limit of $t_0 - t$. The limits, which may be called the weighting time-limits, are $m_1 = 22$ sec for wind speed and $m_2 = 35$ sec for wind direction. Thus the constant, B, can be computed from

$$e^{-Bm} = 0.05 \quad \text{or} \quad B\,m = 2.996.$$

We then have $B_1 = 0.136\ \text{sec}^{-1}$ for wind speed and $B_2 = 0.086\ \text{sec}^{-1}$ for wind direction. These values give the time constants, $B_1^{-1} = 7.4$ sec and $B_2^{-1} = 11.3$ sec, of exponential changes in winds when instantaneous increase or decrease in individual winds takes

place. The wind computed from

$$\tilde{\tilde{W}}_{t_o} = \sum_{t_o-m}^{t_o} W_t \, e^{-B(t_o-t)} \Big/ \sum_{0}^{m} e^{-Bm} \qquad (2)$$

is called in this paper the "weighted wind." It is evident that the variation of weighted winds are usually smaller than those of individual winds and that their changes exhibit a few seconds' time lag because the weighting function varies as follows:

Table I. Exponential weighting functions

Time, $(t_o - t)$	0	5	10	15	20	22	25	30	35 sec
For speed	1.00	0.51	0.26	0.13	0.07	0.05 (weighting time-limit)			
For direction	1.00	0.65	0.42	0.28	0.18	0.15	0.12	0.08	0.05 (limit)

This table indicates that the weighting function decreases to less than 0.5 within several seconds; however, it should be noted that the outputs from the ASN-6 airborne computer do not always give these weighted winds, because the maximum rate of change in the output winds from the computer is restricted to 2.51 deg sec^{-1} for direction and 7.06 kt sec^{-1} for wind speed. As long as the rate exceeds these values, the output simply increases or decreases in linear fashion at the maximum rate until the difference between the latest output wind and the following weighted wind becomes less than the maximum rate mentioned above. The ASN-6 output wind is identified in this paper as the "ASN wind" and is designated by $\tilde{\tilde{W}}$.

These three winds--individual, weighted, and ASN--are identical when their time variations are small. Fig. 3 represents the weighted and ASN winds computed from schematical changes in the individual winds during an 80-sec period. The three winds are identical until 1, when the individual wind started decreasing at a moderate rate. The time of the minimum weighted wind at 3 lags behind point 2. When the individual wind drops sharply along 6, the weighted wind also drops exponentially with considerable time lag, but the ASN wind fails to follow the steep dive, decreasing linearly from 8 to 9. More drastic change is demonstrated by using a rectangular change in the individual wind along the lines connecting 10, 12, 14, and 16. The slow-response ASN direction simply increased then decreased linearly, forming a triangle.

Such rapid change does not always occur unless an aircraft flies through a rainband in which significant attenuation of Doppler beams takes place.

During the wet-beam penetration, M, through a rainband (see Fig. 2), about 30 mi southeast of Flora's eye, near-zero wind speeds were obtained for more than a one-minute period. ASN wind plotted from the computer printout is shown in Fig. 4 by heavy lines connecting open circles. A typical linear change is apparent, especially in the ASN direction, suggesting that rapid changes in wind direction took place while flying through the rainband. The individual winds were computed by solving navigation triangles under the assumption that the antenna was in a null position, and they were then entered on Fig. 4. When the individual and the ASN winds are carefully compared, keeping in mind the fact that the time increases from right to left, it will be found that most of the differences can be explained by the foregoing definitions of winds, with the exception that the changes in the ASN speed when it is near zero are rather difficult to explain. The figure shows that the individual speed started increasing steadily shortly before 1612, in spite of the fact that the ASN speed was zero for more than 20 sec. Nevertheless, the figure represents the typical, fast changes in wind direction and speed measured when an aircraft traverses heavy precipitation in hurricane rainbands.

In view of the fact that the ASN winds as well as the weighted winds include unnecessary smoothing, the following discussion of Doppler winds is based only upon the individual winds computed from true air speed, true heading, drift angle, and ground speed at one-second intervals.

4. Influence of Return Signals from Raindrops upon Doppler-measured Winds.

In his study of rainbands, Gentry (1964) supported the manufacturer's statement that the Doppler system measures the ground velocity. Before 1962, there were practically no measurements showing significant zero Doppler winds. Gray (1965) pointed out that there were ten obvious places in the data he examined where ASN winds were near zero for 10- to 15-second durations, and the use of such data was avoided for his computation of vertical air motion inside hurricanes. These authors equally agreed that a Doppler-measured wind would be zero if four beams lock onto raindrops moving with the winds at the flight level, and they therefore suggested a complete study of such attenuation processes that give rise to the unrealistic winds computed by the APN-82 system.

According to Fujita's (1966) basic research on the four-beam Doppler system, the attenuation of beams can be treated as "wet-beam problems" which can be solved under certain assumptions. We assume that the spectral power of the return signal received by a specific beam can be expressed by a symmetric mound-shaped function,

$$P_{X,\nu} = F\ (M_X, \delta\nu_X, \delta\nu\ ),$$

where $P_{X,\nu}$ denotes the spectral power as a function of $\delta\nu$, the frequency shift of the return signal; and M_X, the maximum spectral power occurring at the center frequency shift, $\delta\nu_X$. F is a function which gives a mound-shaped distribution of $P_{X,\nu}$. The spread of this function is caused mainly by the beam width in the direction perpendicular to the isodops applicable to the backscattering objects designated by the suffix, x. The half-power beam width of APN-82 is 3.5°, according to the system accuracy study by Rinaldi (1965), who made a detailed analysis of the APN-82 system on board RFF aircraft. Thus the half-power occurs at the frequency shift,

$$\delta\nu = \delta\nu_X \frac{\cos(\gamma_0 \pm 1.75°)}{\cos\gamma_0},$$

where γ_0 is the angle between the beam and the Doppler heading in a null position. Using $\gamma_0 = 68°$, we obtain the difference between the center and the half-power frequency shifts, $\delta\nu - \delta\nu_X \doteq 0.08\,\delta\nu_X$. This value indicates that the mound-shaped function decreases to half when 8% of the center frequency shift is either added to or subtracted from the center frequency shift.

When backscattered signals from two groups of objects, X and Y, are received by the four beams, the spectral power affecting each beam consists of the resultant of two mound-shaped curves with two different center frequency shifts, $\delta\nu_X$ and $\delta\nu_Y$. Figure 5 shows the spectral power distribution when two mound-shaped functions are added, thus

$$P_\nu = \phi P_{X,\nu} + (1-\phi) P_{Y,\nu}\ , \qquad (3)$$

where ϕ denotes the fractional contribution of the return signal from X. In this case, the maximum return signals, M_X and M_Y, are considered identical. In reality, however, it is rather difficult to estimate which one is larger, since the ground return depends upon the aircraft altitude and sea-surface conditions. From the top

to the bottom, ϕ was increased from 0.0 to 1.0 at 0.2 intervals.

According to Rinaldi's (1965) report, the frequency tracker determines the center frequency shift, $\delta\nu_X$, when the spectral powers measured by a filter at the frequency shifts, $0.9\,\delta\nu_X$ and $1.1\,\delta\nu_X$, are identical, thus disregarding the other parts of the spectral power distribution. The positions of the frequency tracker are indicated in the figure by black circles. The frequency shift at these positions is the measured frequency shift of a specific beam. The figure reveals that the frequency measured by the frequency tracker increases from $\delta\nu_X$ to $\delta\nu_Y$ as a linear function of ϕ when μ, the signal separation defined by $\mu = |(\delta\nu_X - \delta\nu_Y)/\delta\nu_X|$, is 0.1. When the signal separation is increased to 0.2, the measured frequency shift increases rather slowly, with ϕ increasing until it reaches about 0.5, when it starts to change rapidly. Thereafter, it approaches $\delta\nu_Y$ rather slowly.

When $\delta\nu_Y$ is 40% larger than $\delta\nu_X$, or $\mu = 0.4$, the resultant spectral power forms two separate mounds, thus making it very difficult for the frequency tracker to determine the frequency shift. In such an extreme case, the measured frequency shift will jump from $\delta\nu_X$ to $\delta\nu_Y$, resulting in a very unstable frequency tracking when ϕ is about 0.5, i.e., the beam is half wet. For smaller values of ϕ, the measured frequency shift is not affected by $\delta\nu_Y$. In other words, a measured frequency shift represents either $\delta\nu_X$ or $\delta\nu_Y$.

It should be noted that the preceding discussion is limited to the measured frequency shift for a single beam. The solution of a four-beam Doppler system requires further mathematical development.

We shall now consider that the objects, X and Y, represent, respectively, the ground and the raindrops illuminated by a Doppler beam. If the raindrops are assumed to move horizontally with the environmental air, their horizontal velocity with respect to the beam is identical to the negative value of the true air velocity, $\mathbf{A}$. With the use of the equation of Doppler frequency shift measured by a single beam, derived by Fujita (1966), we write

$$\delta\nu_A = C_o\, A\, \cos(a-\alpha), \qquad (4)$$

and

$$\delta\nu_G = C_o\, G\, \cos(g-\alpha), \qquad (5)$$

where $\delta\nu_A$ and $\delta\nu_G$ are the center frequency shifts due to the raindrops and the ground; G, the ground speed; and C_o, a constant which includes the Doppler frequency

and η_o , the beam nadir angle. The angles, a, g, and α , are the azimuths of the true air velocity, ground velocity, and the Doppler beam respectively.

The signal separation obtained from Eqs. (4) and (5) is written as

$$\mu = \left[\!\left[\frac{\delta V_A - \delta V_G}{\delta V_G} \right]\!\right] = \left[\!\left[\frac{A}{G} \frac{\cos(\alpha - a)}{\cos(\alpha - g)} - 1 \right]\!\right] \qquad (6)$$

where brackets, $[\![\ ]\!]$, denote the absolute value so that μ is always expressed by a positive value. Expressing the azimuth of the Doppler heading in its null position by d_o , we write the azimuths of the four beams as $\alpha_1 = d_o + \psi_o$ (right front beam), $\alpha_2 = d_o - \psi_o$ (left front beam), $\alpha_3 = d_o + \psi_o + 180°$ (left rear beam), and $\alpha_4 = d_o - \psi_o + 180°$ (right rear beam). From these azimuths, the signal separation for each beam is obtained, thus

$$\mu_1 = \mu_3 = \left[\!\left[AG^{-1}\cos(d_o + \psi_o - a)\ \sec(d_o + \psi_o - g) - 1 \right]\!\right]$$

and

$$\mu_2 = \mu_4 = \left[\!\left[AG^{-1}\cos(d_o - \psi_o - a)\ \sec(d_o - \psi_o - g) - 1 \right]\!\right] \qquad (7)$$

When all the beams are completely dry, the Doppler velocity and the ground velocity are equal, permitting us to write $d_o = g$. If all the beams are completely wet, however, the measured Doppler velocity represents the true air velocity and $d_o = a$. During the transition period between these extreme cases, the Doppler heading will indicate an azimuth between a and g. We now express the Doppler heading during this transition period as

$$d_o = g - c\delta, \qquad (8)$$

where $\delta = g - a$ is the drift angle of the aircraft and c, the fraction of the drift angle designating the antenna rotation from the dry-beam position toward the aircraft heading. Using Eq. (8), we reduce Eq. (7) to

$$\mu_1 = \mu_3 = \left[\!\left[AG^{-1}\cos\{\psi_o + (1-c)\delta\}\ \sec(\psi_o - c\delta) - 1 \right]\!\right]$$

and

$$\mu_2 = \mu_4 = \left[\!\left[AG^{-1}\cos\{\psi_o - (1-c)\delta\}\ \sec(\psi_o + c\delta) - 1 \right]\!\right]. \qquad (9)$$

In order to obtain the numerical values of these signal separations, only two types of traverses are considered. They are a longitudinal traverse with a crosswind angle, $\zeta = \alpha - w = 0$ or $180°$, and a normal traverse with $\zeta = 90°$ or $270°$. For these traverses both δ and AG^{-1} can be expressed as unique functions of the ratio, $y = WA^{-1}$, the wind speed divided by the true air speed. Using the following relationships,

$$\begin{aligned} \delta &= 0 && \text{when } \zeta = 0 \text{ or } 180 \\ &= \pm \cos^{-1}\left(1 + y^2\right)^{-\frac{1}{2}} && \text{when } \zeta = 90(-) \text{ or } 270(+), \\ AG^{-1} &= \left(1 \pm y\right)^{-1} && \text{when } \zeta = 0(+) \text{ or } 180(-) \\ &= \left(1 + y^2\right)^{-\frac{1}{2}} && \text{when } \zeta = 90 \text{ or } 270, \end{aligned} \qquad (10)$$

the signal separation given by Eq. (9) can be computed.

The signal separation, μ, is a very important non-dimensional quantity to determine if $\Delta\nu$, the measured frequency shift, varies from $\delta\nu_G$ to $\delta\nu_A$ linearly or non-linearly as a function of ϕ, the fractional contribution of the objects between the Doppler system and the ground. When water droplets attenuate the beam, ϕ is called the "wetness" of the beam.

A generalized variation of the measured frequency shift, $\Delta\nu$, as a function of the wetness of a beam is presented in Fig. 6. It is seen that $\Delta\nu$ varies in proportion to ϕ when μ is smaller than the lower critical value, $\mu_L \fallingdotseq 0.20$, and that is suddenly jumps from $\delta\nu_G$ to $\delta\nu_A$ when μ is larger than the upper critical value, $\mu_H \fallingdotseq 0.30$. For any signal separation above μ_H, the frequency tracker loses the return signal when ϕ reaches the maximum wetness; ϕ_{MAX}; as, for example, at point 1 in the figure. The tracker then sweeps down the frequency shift until it finds the signal from the raindrops at 2. Thereafter a continuous tracking toward A is expected as the wetness increases to 1.0.

When the tracker loses the return signal at 4, the process of finding the signal from the raindrops is rather time-consuming, because $\delta\nu_A$ is larger than $\delta\nu_G$. The system goes into a memory mode at 4, after which the tracker sweeps down to the lowest end of the range, i.e., the 70-kt shift, flying back to a 700-kt shift in 5 sec. It then sweeps down at an exponential rate until a signal is found at 7. The time required to sweep down from the 700-kt to the 70 kt-shift, if there are no detectable signals between them, would be 60 seconds. The process of finding the signal from the ground when ϕ decreases from 1.0 to 0.0 is exactly opposite. The wetness at which the tracker loses the signal in this case is designated by ϕ_{MIN}, the minimum wetness. If the central spectral power at two central frequency

shifts, δv_G and δv_A, is equal, the maximum and minimum wetness distributes on both sides of 50% wetness; thus, $\phi_{MIN} < 0.5 < \phi_{MAX}$.

It should be noted, therefore, that there are three tracking modes, classified according to the magnitude of the signal separation. They are:

(A) linear mode, occurring when $\mu < \mu_L \fallingdotseq 0.2$ and expressed by

$$\Delta v = \delta v_G - \phi (\delta v_A - \delta v_G) , \qquad (11)$$

(B) transient mode, occurring when $\mu_L < \mu < \mu_H$ and

(C) locking mode, occurring when $\mu < \mu_H \fallingdotseq 0.3$ and expressed by

$\Delta v = \delta v_G$ for $\phi < \phi_{MAX}$ while ϕ increases and for $\phi < \phi_{MIN}$ while ϕ decreases,

$\Delta v = \delta v_A$ for $\phi > \phi_{MAX}$ while ϕ increases and for $\phi > \phi_{MIN}$ while ϕ decreases.

Complete evaluation of these three modes is of vital importance in calculating the change in Doppler winds measured under the influence of wet beams.

For linear-mode frequency tracking, the Doppler speed, D, introduced by Fujita (1966) can be expressed as the real part of a complex variable obtained from Eqs. (4), (5), and (11), thus

$$\begin{aligned} D\, e^{i(d-\alpha)} &= G\, e^{-i(g-\alpha)} + \phi \left\{ A e^{-i(a-\alpha)} - G e^{-i(g-\alpha)} \right\} \\ &= G\, e^{-i(g-\alpha)} - \phi\, W^{-i(w-\alpha)} . \end{aligned} \qquad (12)$$

If $\mathbf{R}$, the horizontal velocity of raindrops, and $\mathbf{W}$, the wind velocity, are identical, we write

$$D\, e^{i(d-\alpha)} = G\, e^{-i(g-\alpha)} + \phi R^{-i(r-\alpha)} , \qquad (13)$$

which can be expressed as a vectorial form,

$$\mathbf{D} = \mathbf{G} - \phi \mathbf{R} \qquad (14)$$

Under the assumption that the front and rear beams are uniformly wet, we obtain the Doppler velocities of the four beams

$$D_1 = D_2 = G - \phi_F R ,$$
$$D_3 = D_4 = G - \phi_R R ,$$

where ϕ_F and ϕ_R are the wetness of the front and rear beams, respectively. The Doppler velocity at the null position is thus given by

$$D_0 = G - \frac{\phi_F + \phi_R}{2} R. \qquad (15)$$

In the case of the locking mode, however, the situation is quite different from that of the linear mode. Assuming again that the two front and two rear beams are uniformly wet, the Doppler velocities are expressed by

(I) $D_0 = G$ $\quad \because D_1 = D_2 = D_3 = D_4 = G$ (16)

when ϕ_F and $\phi_R < \phi_{MAX}$ while ϕ increases or
when ϕ_F and $\phi_R < \phi_{MIN}$ while ϕ decreases.

(II) $D_0 = G - \frac{1}{2}R = \frac{1}{2}(G + A)$ $\quad \because D_1 = D_2 = G - R$ & $D_3 = D_4 = G$ (17)

when $\phi_F > \phi_{MAX}$ while ϕ increases or $\phi_F > \phi_{MIN}$ while ϕ decreases and
when $\phi_R < \phi_{MAX}$ while ϕ increases or $\phi_R < \phi_{MIN}$ while ϕ decreases.

(III) $D_0 = G - \frac{1}{2}R = \frac{1}{2}(G + A)$ $\quad \because D_1 = D_2 = G$ & $D_3 = D_4 = G - R = A$ (18)

when $\phi_F < \phi_{MAX}$ while ϕ increases or $\phi_F < \phi_{MIN}$ while ϕ decreases and
when $\phi_R > \phi_{MAX}$ while ϕ increases or $\phi_R > \phi_{MIN}$ while ϕ decreases.

(IV) $D_0 = G - R = A$ $\quad \because D_1 = D_2 = D_3 = D_4 = G - R = A$ (19)

when ϕ_F and $\phi_R > \phi_{MAX}$ while ϕ increases or
when ϕ_F and $\phi_R > \phi_{MIN}$ while ϕ decreases.

Thus the locking mode results in the Doppler velocity expressed by the mean value of G and A.

During transient-mode tracking, a Doppler-measured velocity represents a value between the velocities which would be measured in the linear and locking modes.

Without going through the basic problems of frequency tracking, Fujita (1966) assumed that the influence of the raindrops attenuating a specific beam can be expressed by

$$D = G - kR \qquad (20)$$

where k represents a fraction of the horizontal velocity of the raindrops which contributes to the frequency shift, according to his definition. In his earlier work, he thought that k denoted the degree of beam wetness; but this is true only for the linear mode. In general, this constant, k, is better called the "effectiveness," since it represents a degree of effective contribution of the raindrops to the measured Doppler velocities.

By comparing Eqs. (20) and (14), it may be concluded that $k = \phi$ in the linear mode. In the locking mode, however, k jumps from 0.0 to 1.0 when ϕ increases to ϕ_{MAX} and from 1.0 to 0.0 when ϕ decreases to ϕ_{MIN}. The Doppler velocity is expressed by

$$D_o = G - \tilde{k}R \qquad (21)$$

where $\tilde{k}$ denotes the mean wetness of the front and rear beams, which are uniformly wet. This velocity results in the discrete values corresponding to $\tilde{k} = 0.0$, 0.5, and 1.0.

5. Normal and Longitudinal Traverses with Uniformly-wet Front and Rear Beams.

The signal separations for longitudinal traverses reduced from Eqs. (9) and (10) are

$$\mu_1 = \mu_2 = \mu_3 = \mu_4 = \left[(1 \pm y)^{-1} - 1\right], \qquad (22)$$

where + is used for $\zeta = 0°$(tailwind); −, for $\zeta = 180°$(headwind); and y to denote the ratio, WA^{-1}.

Table II. Signal separation for longitudinal traverses

y	0.1	0.2	0.3	0.4	0.5
Tailwind	0.091L	0.167L	0.231T	0.286T	0.333T
Headwind	0.111L	0.250T	0.429K	0.667K	1.000K

The letters L, T, and K in the table indicate the linear, transient, and locking modes, respectively. The result reveals that the linear mode takes place when y is less than about 0.25 for tailwind and 0.15 for headwind traverses. If a DC-6B with A = 220 kt and a B-57 with A = 500 kt are used for these traverses, the wind speed inside a

rainband must be below about 55 kt and 130 kt, respectively, for tailwind traverses and about 35 kt and 75 kt for headwind traverses in order to obtain $\mu < \mu_L$. Above these wind speeds, the measured frequency shift will be little affected by the return signals from the raindrops until the wetness exceeds 0.5 or 0.6, when the frequency tracker suddenly starts measuring the frequency shift due to the raindrops. Because the directions of true air speed, ground speed, and wind are identical for longitudinal traverses, the Doppler and aircraft headings are also the same. Therefore, the direction of the Doppler wind always indicates that of the true wind, no matter how large the wetness is, as long as the front and rear beams are uniformly wet.

The signal-separation for normal-mode traverses is slightly complicated because it depends upon both y and c in Eqs. (9) and (10). The numerical values of μ are presented in the two following tables in which the linear, transient, and locking modes are identified by the letters L, T, and K, respectively.

Table III. Signal separation[1], $\mu_1 = \mu_3$ for $\zeta = 90°$ and of $\mu_2 = \mu_4$ for $\zeta = 270°$

y	0.1	0.2	0.3	0.4	0.5
when c = 0.0	0.081L	0.137L	0.169L	0.177L	0.166L
0.2	0.084L	0.152L	0.200L	0.229T	0.240T
0.4	0.088L	0.167L	0.235T	0.290T	0.332T
0.6	0.092L	0.184L	0.275T	0.364T	0.449K
0.8	0.096L	0.203T	0.322T	0.456K	0.609K
1.0	0.101L	0.224T	0.378T	0.576K	0.842K

Table IV. Signal separation[2], $\mu_2 = \mu_4$ for $\zeta = 90°$ and of $\mu_1 = \mu_2$ for $\zeta = 270°$

y	0.1	0.2	0.3	0.4	0.5
when c = 0.0	0.100L	0.214T	0.334T	0.453K	0.566K
0.2	0.097L	0.201T	0.306T	0.408K	0.503K
0.4	0.093L	0.188L	0.281T	0.368T	0.448K
0.6	0.090L	0.176L	0.257T	0.332T	0.399T
0.8	0.087L	0.165L	0.236T	0.299T	0.355T
1.0	0.084L	0.155L	0.215T	0.268T	0.314T

Footnote 1 and 2. Tracking modes in these tables are for a circular beam with 3.5° width. APN-82 beams with 30° beam fan-angle would broaden the mound-shaped return signals considerably when the signals are received from particles moving not in the direction of Doppler heading, resulting in an appreciable increase in both μ_L and μ_H.

Illustrated in Fig. 7 are the changes in ϕ, the wetness, and k, the effectiveness, which would occur during normal traverses with three different values of y. The rainband extends between 4 and 9, resulting in an increase of the wetness, ϕ_F, at point 1 outside the rainband when the end of the front beams intersects the rain at sea level. Thereafter, the wetness increases more or less in linear fashion until 3, where the front beams lock onto the raindrops. Between 3 and 4, the rear beams are still dry until the aircraft enters the rain at 4. The wetness of the rear beam gradually increases to point 6 and the beam remains soaking wet ($\phi = 1.0$) until 10. The drying processes of all the beams are self-explanatory.

Despite the fact that the variation of ϕ_F and ϕ_R is identical in all three traverses with different y, the effectiveness, k, varies quite differently because y alters the signal separation, resulting in a change in the tracking mode. The heavy dashed lines represent the estimated variation of the mean $\tilde{k} = \frac{1}{2}(k_F + k_R)$ in these traverses. It is evident that the effectiveness and the wetness are almost identical when $y = 0.2$, which corresponds to a 44-kt wind for a DC-6B and to a 100-kt wind for a B-57. Above these wind speeds with $y = 0.2$, the mean effectiveness stays low between 1 and 2, where it increases suddenly to 0.5. The mean effectiveness remains 0.5 for a long time until the rear beams suddenly lock onto the raindrops at 5, when the wetness of the rear beams reaches ϕ_{MAX}, thus completely losing the Doppler signals from the ground.

These complicated changes in the effectiveness may be expressed as $\tilde{k} = \tilde{\phi}$ when y is less than about 0.2; and the discrete values, $\tilde{k} = 0.0$, 0.5, and 1.0, are likely to occur when $y > 0.2$, thus avoiding in-between values even though ϕ changes linearly.

6. Solution of Doppler Velocity involving both Horizontal and Vertical Velocities of Raindrops.

Doppler velocities affected by either horizontal or vertical velocities of raindrops have already been obtained by Fujita (1966). We shall consider a more general case in which both horizontal and vertical velocities are included simultaneously. The vertical motion of the aircraft may be neglected because it would affect the frequency shifts equally and simultaneously.

We may write the total frequency shift for each beam under the influence of both horizontal and vertical velocities of raindrops as

$$\Delta v_1' = C_o \; D_1 \cos (d_1 - \alpha_1) - C_o \; K_1 \; R_1' \cot \eta_o ,$$
$$\Delta v_2' = C_o \; D_2 \cos (d_2 - \alpha_2) - C_o \; K_2 \; R_2' \cot \eta_o ,$$
$$\Delta v_3' = C_o \; D_3 \cos (d_3 - \alpha_3) - C_o \; K_3 \; R_3' \cot \eta_o ,$$
$$\Delta v_4' = C_o \; D_4 \cos (d_4 - \alpha_4) - C_o \; K_4 \; R_4' \cot \eta_o , \qquad (23)$$

where C_o is a constant; D, the Doppler speed applicable to each beam; d, the azimuth of each Doppler velocity; k, the effectiveness; R', the vertical velocity; and η_o, the beam nadir angle, which is 30.50° for APN-82. Assuming that the front and rear beams are uniformly wet, thus

$$D_F = D_1 = D_2, \; d_F = d_1 = d_2, \; k_F = k_1 = k_2, \text{ and } R_F' = R_1' = R_2' ,$$
and $$D_R = D_3 = D_4, \; d_R = d_1 = d_2, \; k_R = k_3 = k_4, \text{ and } R_R' = R_3' = R_4' ,$$

then, the balanced condition of the antenna at the null position,

$$\Delta v_1' - \Delta v_3' = \Delta v_2' - \Delta v_4' , \qquad (24)$$

can be written as

$$D_F \cos (d_F - \alpha_1) - k_F R_F' \cot \eta_o - D_R \cos (d_R - \alpha_3) + k_R R_R' \cot \eta_o$$
$$= D_F \cos (d_F - \alpha_2) - k_F R_F' \cot \eta_o - D_R \cos (d_R - \alpha_4) + k_R R_R' \cot \eta_o , \qquad (25)$$

which is reduced to

$$D_F \cos (d_F - \alpha_1) - D_F \cos (d_F - \alpha_2) = D_R \cos (d_R - \alpha_3) - D_R \cos (d_R - \alpha_4). \qquad (26)$$

Substituting for the four azimuths in this equation

$$\alpha_1 = d_o + \psi_o , \quad \alpha_2 = d_o - \psi_o , \quad \alpha_3 = d_o + \psi_o + 180°, \text{ and } \alpha_4 = d_o - \psi_o + 180°,$$

we have

$$D_F \cos(d_F - d_o - \psi_o) - D_F \cos(d_F - d_o + \psi_o) + D_R \cos(d_R - d_o - \psi_o) - D_R \cos(d_R - d_o + \psi_o) = 0 \qquad (27)$$

This equation indicates that the Doppler-measured azimuths obtained with and without the vertical velocity, R', are identical, that is

$$d_o' = d_o = \text{azimuth of } (D_F + D_R), \qquad (28)$$

where d_o' denotes the azimuth measured with the vertical velocity.

The magnitude of the Doppler velocity, $\mathbf{D}_o'$, including the vertical velocity, is obtained by combining

$$\left[\Delta v'\right]_3^1 = \left[\Delta v'\right]_4^2 = 2\ C_o\ D_o'\ \cos\psi_o \qquad (29)$$

with Eqs. (25) and (27). Thus we have

$$2\ D_o' = \left[\!\left[\ \mathbf{D}_F + \mathbf{D}_R\ \right]\!\right] - (k_F R_F' - k_R R_R')\cot\eta_o \sec\psi_o\ , \qquad (30)$$

which is reduced, when $R_F' = R_R' = R'$, to

$$2\ D' = 2\ D_o - 2\ \Delta D_o' \qquad (31)$$

where

$$\Delta D_o' = \tfrac{1}{2}(k_F - k_R)\ R'\cot\eta_o\ \sec\psi_o \qquad (32)$$

indicates the change in wind speed caused by the vertical velocity of the raindrops. It should be noted that the change may be either positive or negative, depending upon the signs of $k_F - k_R$ and R' , positive for falling raindrops.

A graphical solution of the problem is presented in Fig. 8. A wet-beam triangle defines the wet-beam Doppler velocities, $\mathbf{D}_F$ and $\mathbf{D}_R$. In this case, the effectiveness of the horizontal velocity of the raindrops is much larger for the front beams than for the rear beams. The double-size navigation triangle formed by the three sides, $2\mathbf{A}$, $2\mathbf{W}$, and $2\mathbf{G}$, gives the wind velocity, $\mathbf{W}$, measured under dry-beam conditions. When the beams get wet, the balance of the differential frequency shift is disturbed and the antenna rotates through the nulling process until its heading comes in line with PX, the wet-beam Doppler heading. If R' is zero, the length, $\overline{PX}$, indicates twice the Doppler-measured speed. When the raindrops are falling or rising, $\Delta D_o'$ is subtracted from D_o without changing its azimuth. Thus the navigation triangle involving beams wet with falling raindrops becomes distorted into ΔPYL. The Doppler wind thus measured is expressed by half of the vector connecting L with Y.

During a wet-beam traverse of a rainband, the Doppler-measured winds undergo rather complicatedbut systematic changes which can be explained through a careful examination of the wet-beam processes of the front and rear beams. Adopting the same numbering system used in Fig. 7, a schematic wet-beam process

in Fig. 9 will be discussed. The initial navigation triangle in the figure consists of three sides, **A** , **G** , and **W** . When the front beams start to become wet at point 1, the end of the wet-beam vector wind starts moving toward 2 in the direction of the positive arrows if $R' > O$. The direction reverses into that of the negative arrows if $R' < O$. This discussion, however, is based upon the assumption that $R' > O$, i.e., the raindrops are falling.

In the linear mode, the wetness of the front beams as well as the effectiveness gradually increase to 3, where both ϕ and k reach 1.0. For the transient and locking (non-linear) modes, an abrupt increase in the effectiveness takes place at 2, where the frequency tracker loses the signals from the ground and begins to lock onto the raindrops. The effectiveness of the front beams remains 1.0 (soaking wet) until 7, where the wetness starts decreasing. Between 7 and 9, the edge of the rainband, the effectiveness decreases either in linear fashion or abruptly, depending upon the tracking modes. In similar manner, the wetness of the rear beams changes until it becomes zero at 12, where the wet-beam wind ends.

The cycle produced by the end of the wet-beam wind vector, originating at L, is called the "wind-velocity cycle." As a result of the change in effectiveness, the cycle is completed by following the numbers, 1, 2, ... 12 along either the full or dashed lines designating the cycle. These lines represent the cycles in the linear and non-linear tracking modes, respectively.

Even though the variation of the effectiveness as well as of the wind-velocity cycles changes considerably according to the linear, transient, and locking modes, there is one thing common to all: that is the uniqueness of the Doppler winds measured with front beams locked onto the raindrops (3 and 4), four locked beams (6 and 7), or rear locked beams (9, 10). The Doppler winds measured under these conditions are not affected by the tracking modes, no matter how they vary.

Shown in Fig. 10 is the change in wet-beam winds obtained from the wind-velocity cycle in Fig. 9, assuming that $R' > O$ (the raindrops are falling). The numbers 1 through 12 indicate the significant points as identified at the bottom of the figure. The wind velocities and the cycle to be obtained in the linear mode appear in full lines and those in the non-linear modes, in heavy dashed lines. It is seen that the winds measured between 3 and 4 (locked front beams), 6 and 7 (all beams locked), and 9 and 10 (locked rear beams) are independent of the tracking modes.

In order to clarify the wind-velocity cycles in simulated traverses, three cases are presented in Fig. 11. In all cases, the rainbands extend from 4 to 9,

accompanied by wet-beam measurements beginning at 1 and ending at 12. Case I represents a traverse in which the 1.0 wetness of the front beams starts decreasing before the rear beams become completely wet. At no period, even momentarily, do all four beams lock onto the precipitation when the tracking is made in the linear mode. In the transient or locking modes, however, all the beams lock onto the raindrops for a short time, resulting in a zero Doppler wind. The patterns of the wet-beam Doppler winds can be seen more clearly in Fig. 12 in which the vector variation of winds in the linear mode (lower) and the non-linear modes (upper) is presented. All winds are obtained from the wind-velocity cycle of Case I, Fig. 11. Because the vertical velocity of the raindrops was chosen as negative (upward), the wet-beams winds give the impression that they are converging toward the rainband. This pattern is opposite from that involving positive vertical velocity (see Fig. 10), which is characterized by diverging wet-beam winds from the rainband region.

Returning to Fig. 11, Case II indicates that the wetness of the front beams reaches 1.0 at the forward edge of the rainband. Within the rainband, the wetness gradually decreases to zero at the rear edge. In this case, the wind-velocity cycle is a triangle. Case III involves wetness reaching up to 0.5, which is not large enough to result in the locking of beams, since the frequency tracker does not lose the signals from the ground if it operates in a non-linear mode. In the linear mode, however, a small wind-velocity cycle appears, resulting in a minor change in the wind velocity.

7. Application of Wet-beam Problems in the Computation of Vertical Velocity of Raindrops.

It has been shown in Eqs. (31) and (32) that $\Delta D'$, the difference between the Doppler velocities, measured under the influence of the horizontal velocity only and the horizontal and vertical velocities combined, is proportional to R', the vertical velocity of the raindrops. Solving Eq. (32) with respect to R', we have

$$R' = \frac{2\Delta D_o' \tan\eta_o \cos\psi_o}{k_F - k_R} , \qquad (33)$$

where $\eta_o = 30.50°$ denotes the beam nadir angle and $\psi_o = 42.43°$, the beam horizontal angle; and k_F and k_R, the effectiveness applicable to the front and rear beams, respectively. Since the Doppler winds are not affected by the tracking modes when

$k_F = 1.0$ and $k_R = 0.0$ (locked front beam)

or $k_F = 0.0$ and $k_R = 1.0$ (locked rear beam),

Eq. (33) can be reduced to

$$R' = 2\,\Delta D_o' \tan\eta_o \cos\psi_o \fallingdotseq 0.866\,\Delta D_o' \quad \text{(locked front beam)},$$

$$R' = -2\Delta D_o' \tan\eta_o \cos\psi_o \fallingdotseq -0.866\,\Delta D_o' \quad \text{(locked rear beam)}. \qquad (34)$$

This result indicates that $\Delta D_o'$ is proportional to the vertical velocity of the raindrops and that the sign of $\Delta D_o'$ reverses, depending upon which beams are completely wet.

The azimuth of the Doppler-measured velocity under these locked-beam conditions is obtained by connecting P (in Fig. 13) with M, the midpoint on the wind-velocity vector. The magnitudes of $\Delta D_o'$ can thus be obtained by plotting the ends of the wet-beam wind vectors, originating at L, from E_1 for the dry-beam wind on the approaching side of the rainband, to E_{12} for the wind on the other side. If the dry-beam winds on both sides of the rainband are identical, a closed wind-velocity cycle will be completed. In reality, however, some difference between the positions of E_1 and E_{12} is inevitable. Nevertheless, the value $\Delta D_o'$ can be measured on the azimuths, $P_1 M_1$ and $P_{12} M_{12}$, with an accuracy of a few knots or about 1 or 2 m sec^{-1}. Should the distances, E_1 and E_{12}, be very large, the reasonable wind velocities at the times of F and R must be interpreted from the two vector winds, LE_1 and LE_{12}.

An example of the vertical velocity determination, using the wet-beam winds obtained during the traverse "M" in Fig. 2, is presented in Fig. 14. The true air velocity was kept to about 205 kt, while the dry-beam wind on the approaching side, $W_1 = 60$ kt, changed into $W_{12} = 68$ kt on the other side of the rainband. The wind-to-air-speed ratio was, therefore, $y_1 = 0.29$ and $y_{12} = 0.33$, indicating that the winds were measured mostly in the transient mode. Measured directly from the figure are $\Delta D_o' = -8$ kt and $\Delta D_o' = -34$ kt, when the front and the rear beams are locked, respectively. The vertical velocities of the raindrops, computed from Eq. (34), are

$R_1' = -7.0$ kt on the approaching side

and $R_{12}' = +29.5$ kt on the other side.

The airplane traversed the rainband toward the hurricane center. The results thus obtained reveal that the raindrops near the outer wall (away from the center) were rising at 7.0 kt or 3.5 m sec^{-1}, while those near the inner wall were falling at 29.5 kt or 15 m sec^{-1}.

Since raindrops disintegrate when their diameter increases beyond about 10 mm, with a terminal velocity of about 10 m sec^{-1}, it is necessary for the environmental air to descend at a rate faster than 5 m sec^{-1} in order to permit the raindrops to fall with such velocity. Near the outer wall of the rainband, on the other hand, an updraft of up to 13 m sec^{-1} must be in existence if the drop sizes exceed 5 mm.

The vertical velocities for all traverses shown in Fig. 2 were computed from the wind-velocity cycles. Not a single case indicated a "straight-line cycle," which is expected when the raindrops are suspended in the updraft. In fact, such a straight-line cycle can be identified immediately because the increase or decrease in the wet-beam wind speeds takes place in the direction of the winds outside the rainband. Figure 15 presents a summary of the computed vertical velocities during the normal traverses identified with the letters A, F, G, J, K, N, and O (see Fig. 2). Of interest are the relatively constant values of R' near the inner eye wall, while they vary appreciably between positive and negative values near the outer wall. The average vertical velocity, however, was about 3 m sec^{-1} near the inner wall and zero near the outer wall. This evidence suggests that the vertical velocity of the air near the outer wall probably fluctuates between -5 to +25 m sec^{-1} if the raindrops are between 5 and 10 mm in diameter. In contrast to such a wild variation, the inner portion of the eye wall was characterized by a more or less uniform updraft of 5 m sec^{-1} during the period of the traverses under discussion.

As a measure of the wet-beams effects during a rainband traverse, a stream function of the error winds was computed for each normal traverse, using the formula,

$$\psi' = \int_{t_1}^{t_{12}} (W - W') \, A \, dt \, , \qquad (35)$$

where t_1 and t_{12} denote the beginning and end times of a wet-beam traverse. When the difference between the dry-beam wind, W, and the wet-beam wind, W', appears for an extended period during flight at the true air speed, A, the stream function of the error winds, ψ', results in a large value. The magnitude of ψ' is thus a

measure of the integrated effects of a rainband upon the Doppler-measured wind. When the computed values of ψ' and R' near the outer wall were compared in Fig. 13, it was found that they are more or less proportional to each other, suggesting that the updraft near the outer wall intensifies when this stream function increases.

8. Conclusions

As a part of the effort in solving the problems of zero winds measured by an APN-82 Doppler wind system, a complete solution of the Doppler winds under the influence of both horizontal and vertical velocities has been undertaken. It was found that the Doppler heading in the null position is not affected by the vertical motion of the raindrops as long as two adjacent beams are uniformly wet during the measurement. Thus the vertical velocity of the raindrops alters the Doppler-measured speed rather than the direction.

Another interesting fact revealed in this study is the change in the modes of frequency tracking, which vary according to a new parameter called the "signal separation." The increment in the measured frequency shift is proportional to the wetness of a beam when the signal separation is small, as in the measurement involving slow-moving raindrops. Near the central regions of a hurricane, where the frequency shifts of the return signals from the ground (sea surface) and the raindrops are widely separated, the signal separation is so large that the frequency tracker locks onto the ground signal until it is entirely lost. Thereafter, the tracker sweeps the frequency-shift range in order to lock onto the signal from the raindrops. Such a mode of tracking, called the locking mode, enables the tracker to lock onto either the ground or the raindrops.

Because a Doppler wind system uses four beams for frequency-shift determination, the system as a whole does not determine either ground or true air velocity; but a few discrete velocities can be obtained, depending upon the number of beams locking onto the raindrops. A solution of the Doppler velocity determined with uniformly-wet adjacent beams gives two median-intensity winds measured with either front or rear beams locking onto the raindrops. These winds are not affected by the tracking modes, and their velocities are used in computing the vertical velocity of the raindrops.

Several computations of the vertical velocity revealed that the results obtained are within the limit of expectation, varying significantly according to the inner or outer portion of an eye-wall rainband. It is expected that the wind data from a well-planned normal traverse will permit us to compute the fall velocity of the raindrops

with an accuracy of 1 or 2 m sec^{-1} if the wet-beam winds drop to less than half of the dry-beam winds measured outside the rainband.

For actual application to hurricanes and possibly to thunderstorms, it is necessary to solve further problems of wind measurement under various combinations of wet beams. In the case of a "fly-by" measurement near an active thunderstorm, it might be feasible to let two side beams lock onto the heavy precipitation so that the fall velocity characteristics of the in-cloud raindrops could be determined. There are a large number of other experiments that might be performed by an APN-82 system; but a further, complete evaluation of the system in cooperation with electronic engineers, system analysts, and flight engineers is necessary.

Acknowledgements: The authors are very grateful to the staff members of Research Flight Facilities, Environmental Science Services Administration, especially to Mr. Harlan Davis, who assisted the authors in various phases of the basic research reported in this paper. Sincere appreciation is also due to Mr. Leonard D. Rinaldi of the Rinaldi Data Processing Consultants Inc., New York City, who made a detailed analysis of RFF's APN-82 system and ASN-6 computer, thus clarifying important questions pertaining to the function of the wind system.

REFERENCES

Fujita, T., 1966: Accurate calibration of Doppler winds for their use in the computation of mesoscale wind fields. Mon. Wea. Rev., 94, 19-35.

Gentry, C., 1964: A study of hurricane rainbands. Nat. Hur. Res. Lab. Report No. 69, 85 pp.

Gray, W., 1965a: Calculation of cumulus vertical draft velocities in hurricanes from aircraft observations. J. Appl. Meteor., 4, 463-474.

Gray, W., 1965b: On the scales of motion and internal stress characteristics of the hurricane. Nat. Hur. Res. Lab. Report No. 73, 121 pp.

Rinaldi, L., 1965: RFF/APN-82 system accuracy study report. Rinaldi Data Processing Consultants, Inc., New York, N. Y., 15 pp.

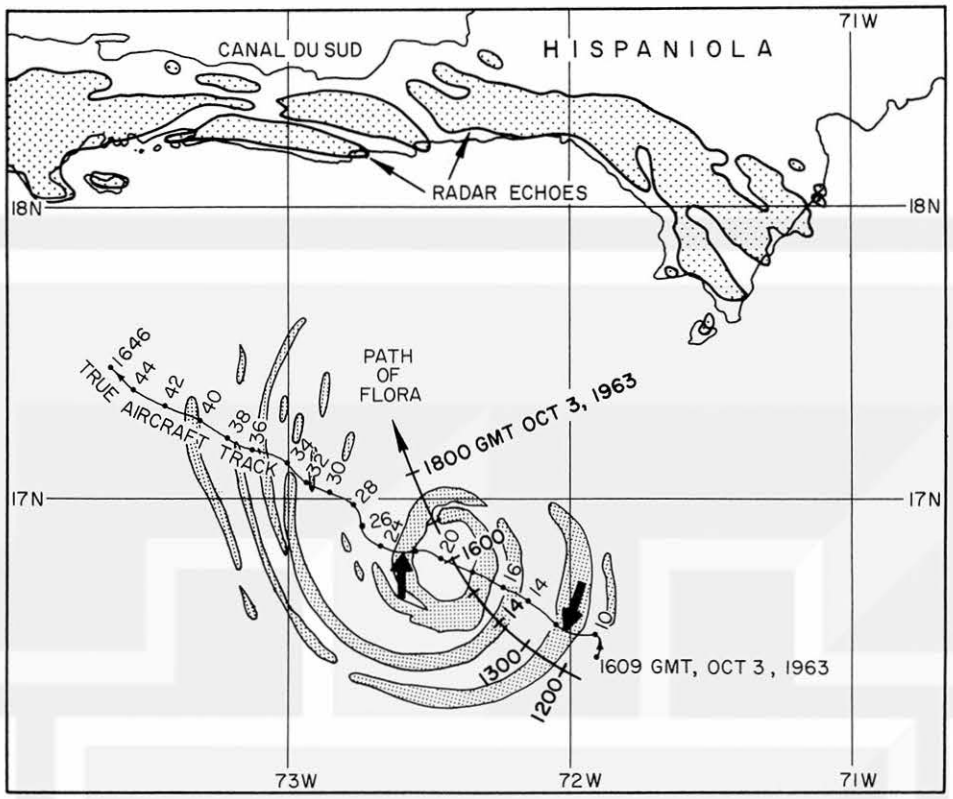

Fig. 1. Rainbands of Hurricane Flora of October 3, 1963, located to the south of Hispaniola. The aircraft positions between 1609 and 1646 GMT, determined from ground echoes from Hispaniola, are shown by black dots connected by a thin line. The zero Doppler winds occurred between 1611 and 1612 and at 1622.5 GMT, indicated by triangles.

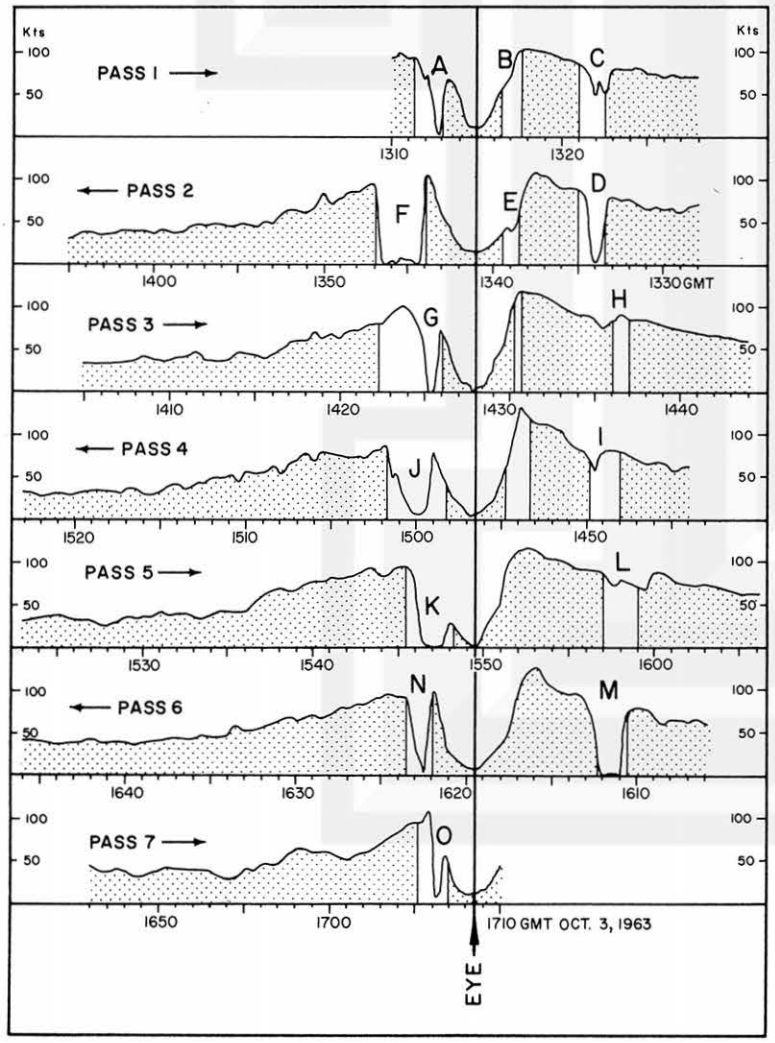

Fig. 2. Variation of wind speed measured during seven normal traverses through the rainbands of Flora of October 3, 1963. The profiles of wet-beam winds are identified by letters A through O. The aircraft went through the eye in each pass.

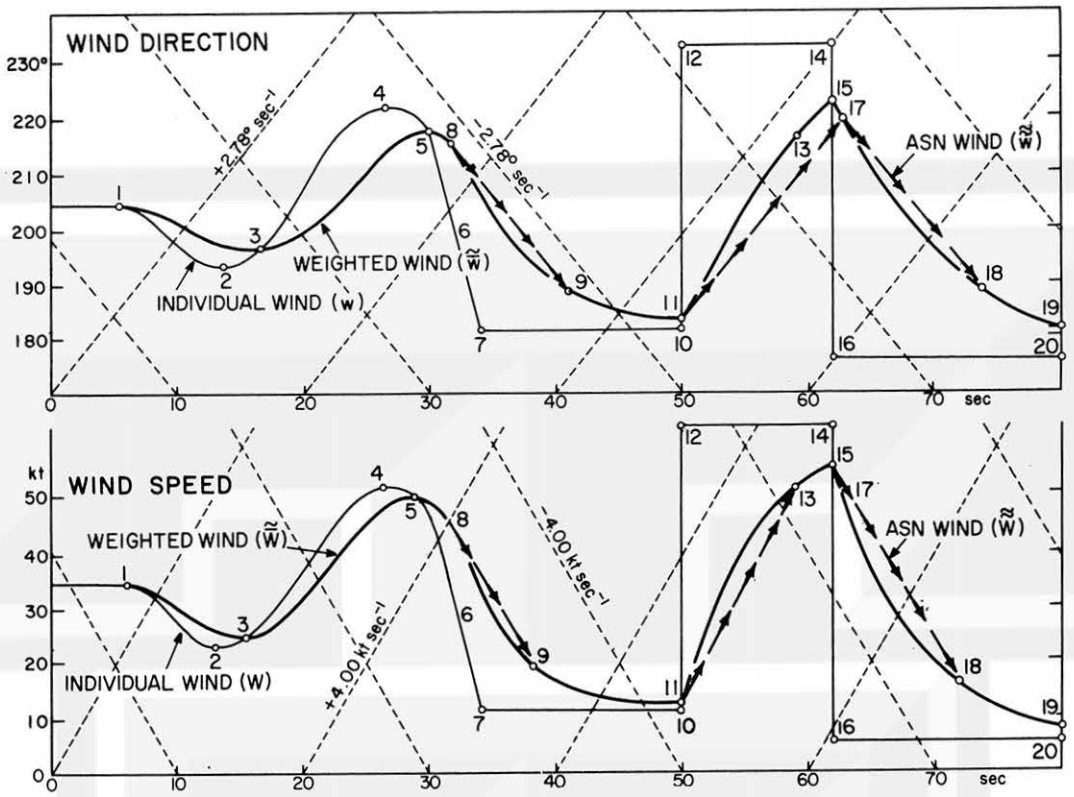

Fig. 3. Schematical diagram showing the difference in the direction and speed of individual, weighted, and ASN winds. The diagonal dashed lines indicate the maximum rate of increase and decrease of the ASN winds.

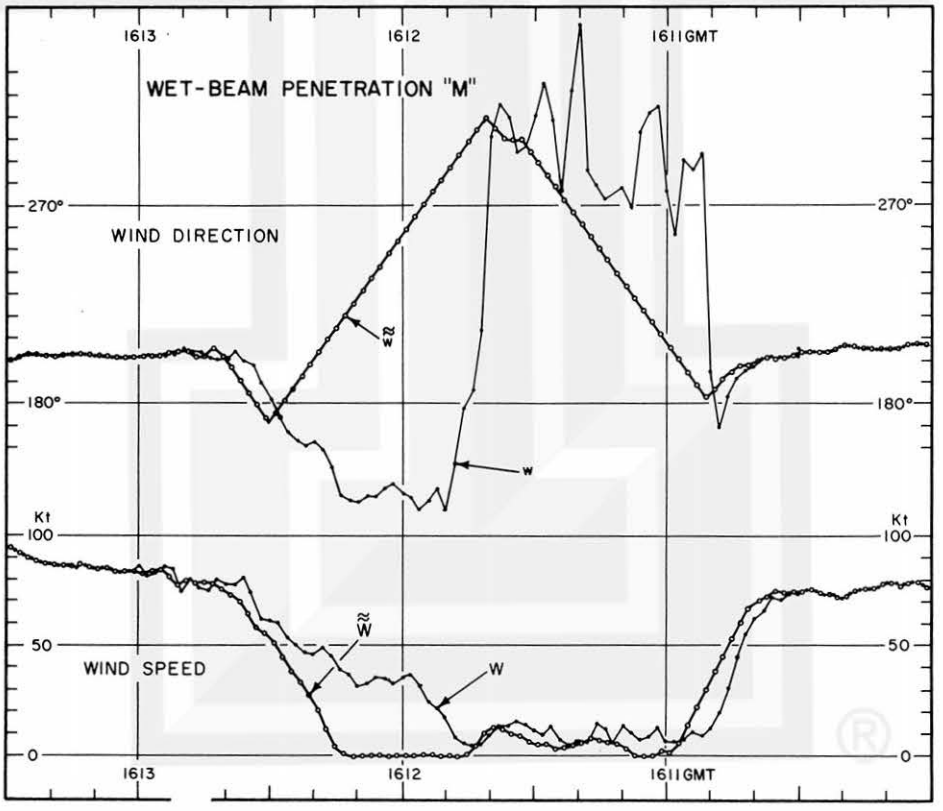

Fig. 4. The difference between the individual winds computed from the original input data and the ASN winds appearing in the printout from the airborne computer. The wet-beam penetration, "M", identified in Fig. 2, was used for computation.

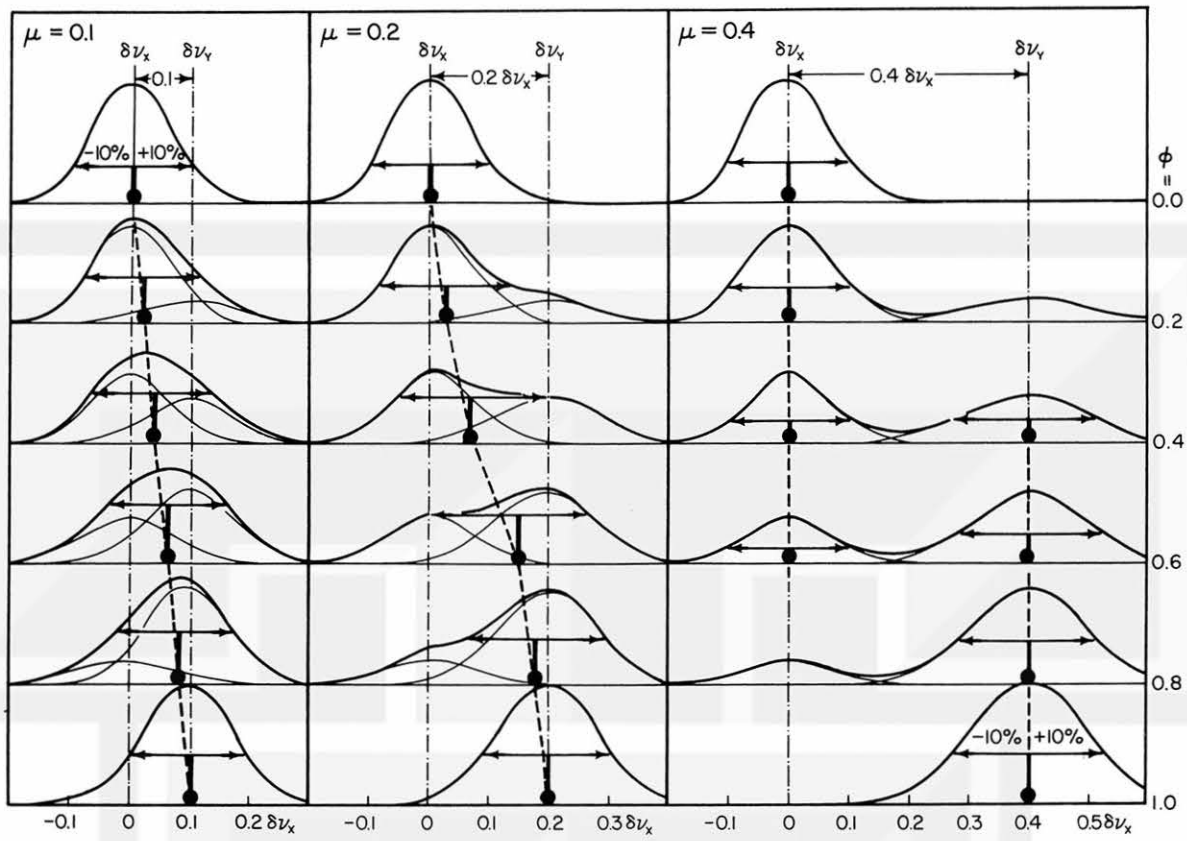

Fig. 5. Schematical diagram showing the superimposition of return signals from two backscattering objects, X and Y. The spectral powers received from these two objects are mixed by using a parameter, ϕ, which is identified as the "wetness" when a beam attenuation is caused by water droplets. Double arrowheads indicate the frequency shifts and the return signals used by the frequency tracker for shift determination. These shifts correspond to values 10% higher and lower than those to be determined by the frequency tracker. Note that the tracker does not measure the shift corresponding to the maximum return signal.

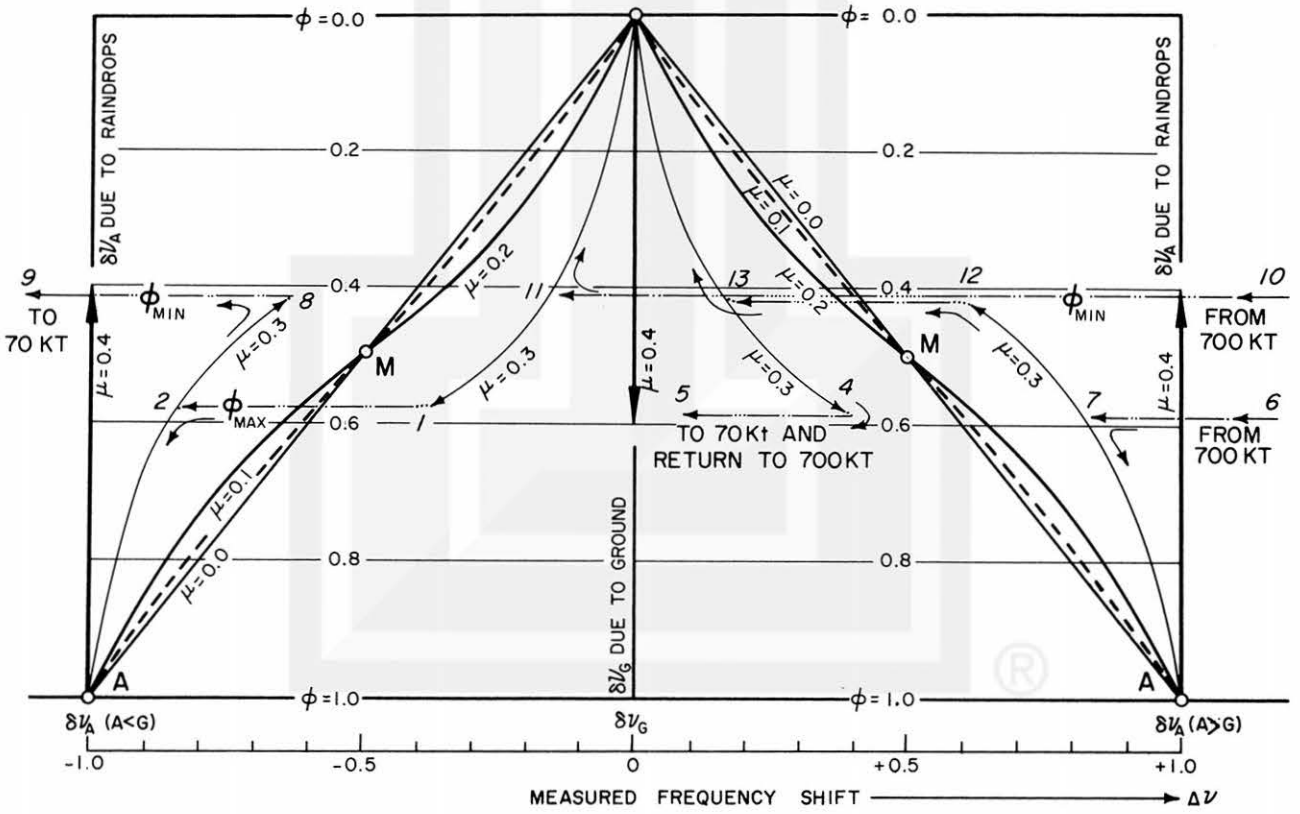

Fig. 6. Variation of the measured frequency shift, $\Delta\nu$, as the wetness of a beam increases from 0.0 to 1.0. Depending upon the value of μ, the signal separation, the tracking mode changes to linear, transient, and locking modes. The last two modes are called non-linear modes.

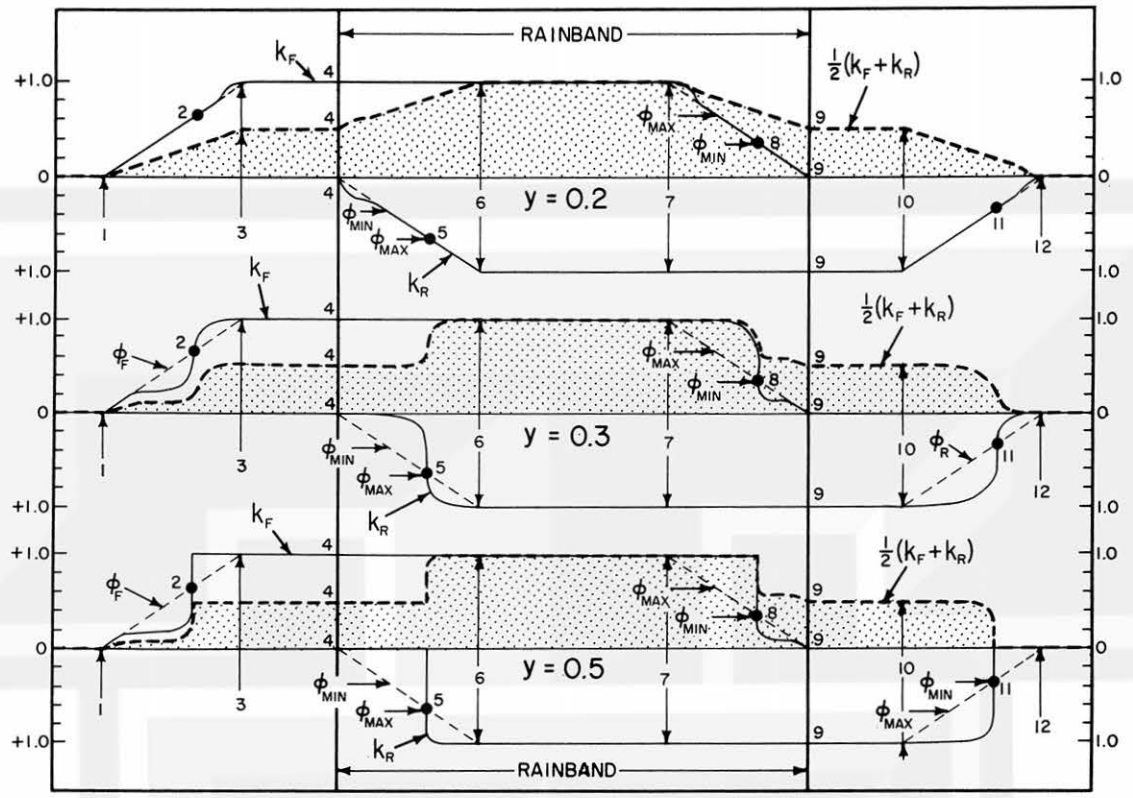

Fig. 7. Schematical variation in k, the effectiveness, when an aircraft makes a normal traverse of a rainband. From the top diagram to the bottom, $y = WA^{-1}$ was increased from 0.2 to 0.3 to 0.5 to show the changes in tracking mode. In all traverses, identical wetness values were used. The rainband exists between 4 and 9, and the wet-beam effects extend from 1 to 12.

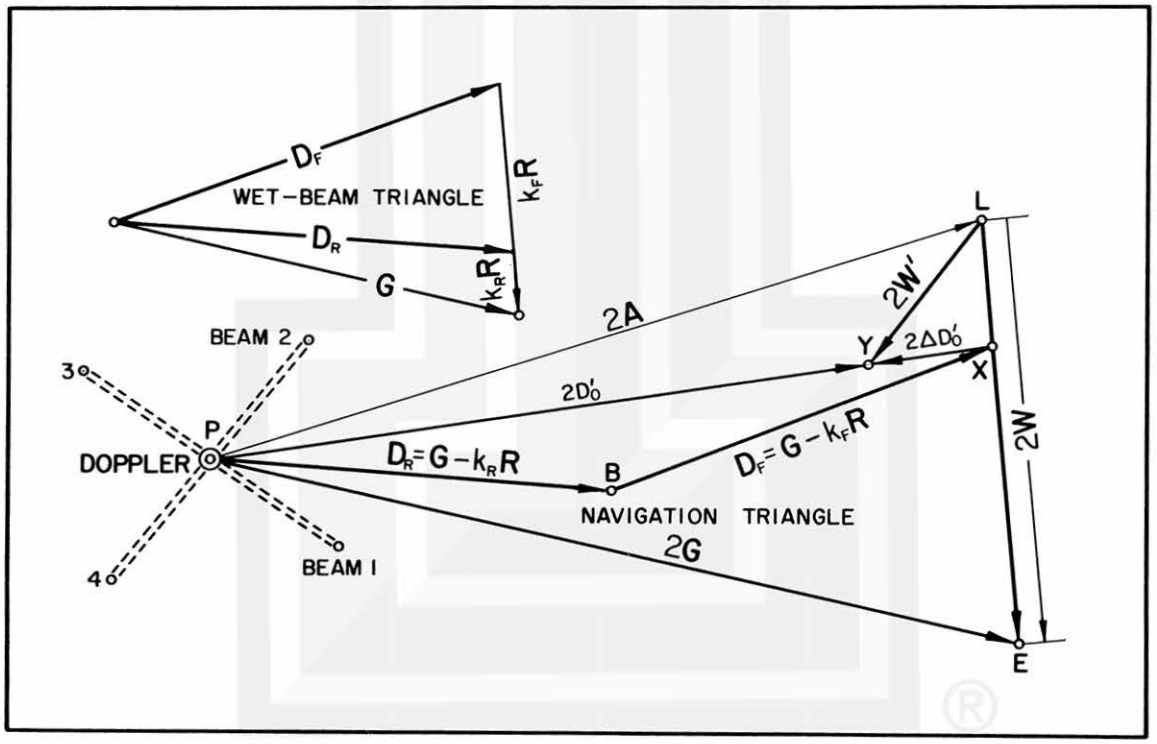

Fig. 8. Graphical representation of a navigation triangle, ΔPLY, affected simultaneously by horizontal and vertical velocities of the raindrops. If no vertical motion exists, the navigation triangle changes into ΔPLX. The vertical velocity thus results in the difference $\overline{XY}$, which, in turn, can be used to calculate the vertical velocity.

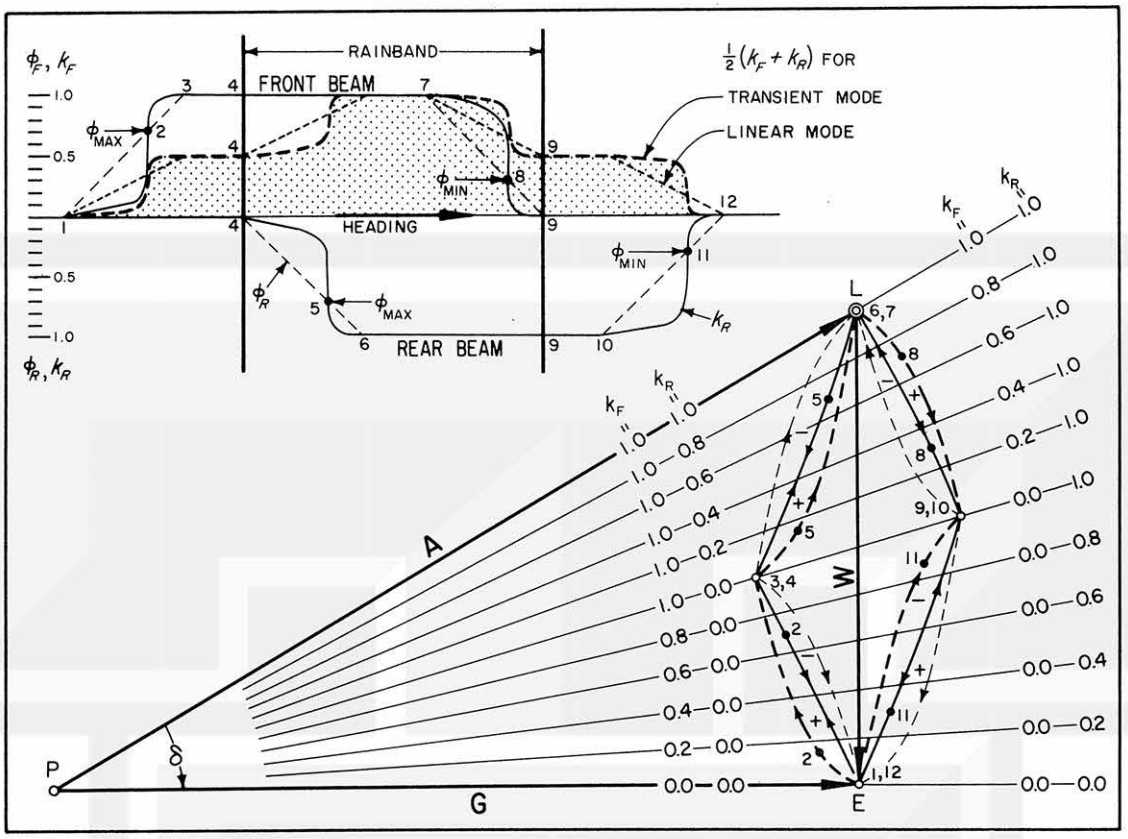

Fig. 9. Wind-velocity cycles completed when an aircraft traverses a rainband attenuating Doppler beams. Shown in the upper left is the variation of wetness and effectiveness during a normal traverse. The cycle is completed in the direction of the positive arrows when the raindrops are falling. If they are rising, the cycle follows the direction of the negative arrows.

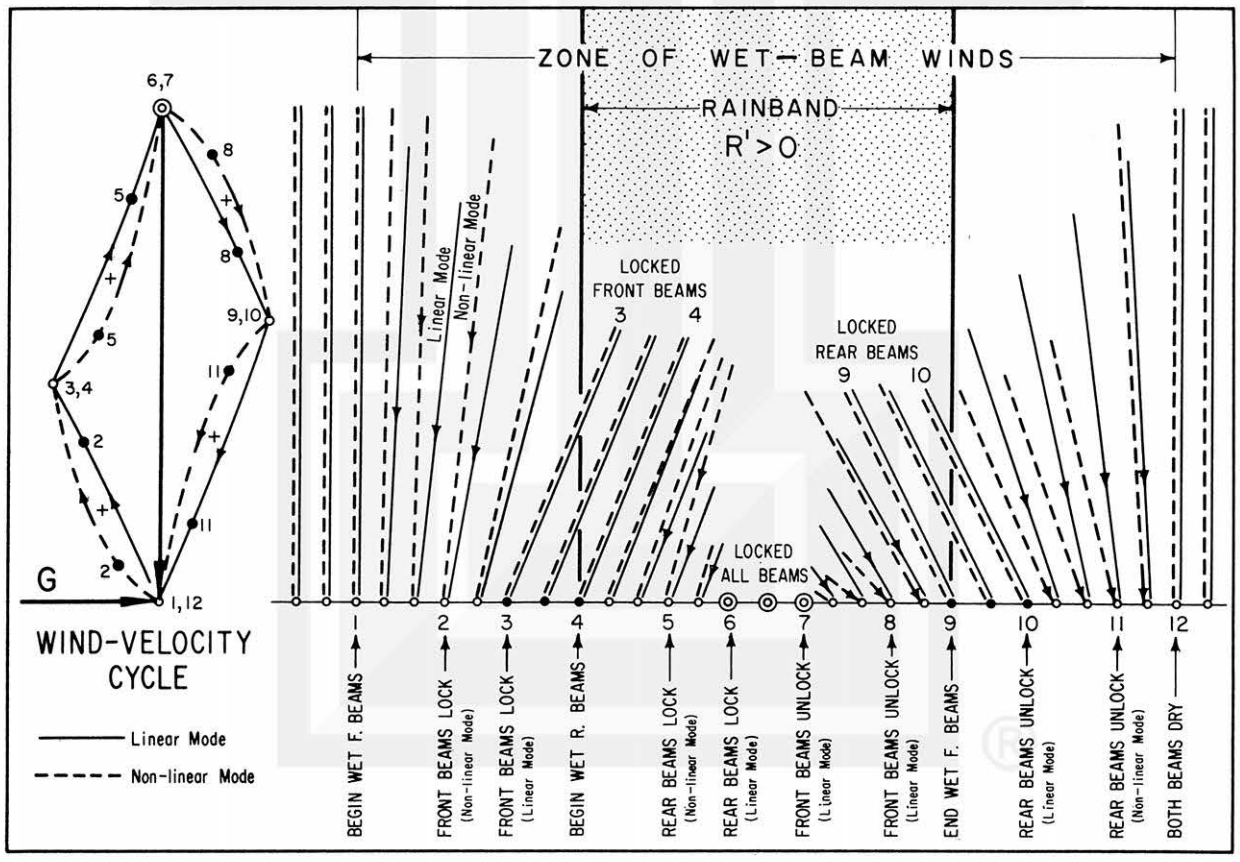

Fig. 10. An example of the change in wind direction and speed during a normal traverse across a rainband with falling raindrops. Note that the width of the wet-beam winds is much broader than that of the rainband and that the falling raindrops give the impression that the winds diverge from the rainband. It will be seen in Fig. 12 that a fictitious converging wind field appears as a result of the rising motion of the raindrops.

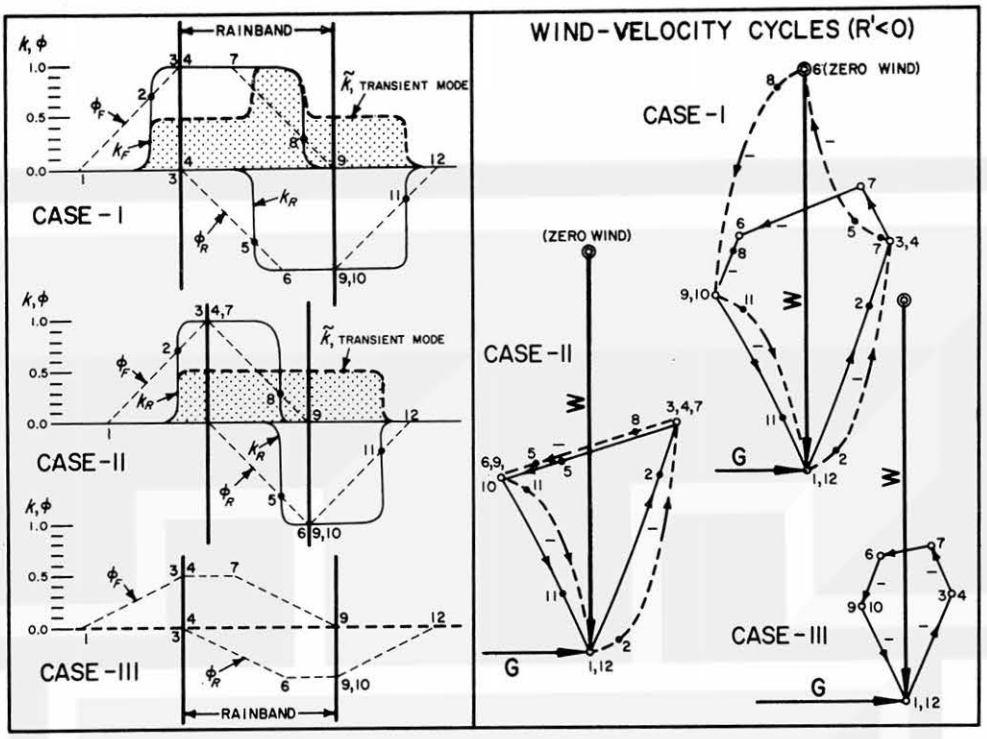

Fig. 11. Three model cases of normal traverses. Case I denotes a relatively narrow rainband with high concentration of raindrops; Case II, a very narrow rainband with similar concentration; and Case III, a relatively narrow rainband with low concentration of raindrops, giving rise to up to 0.5 wetness. The wind-velocity cycles corresponding to these cases appear to the right.

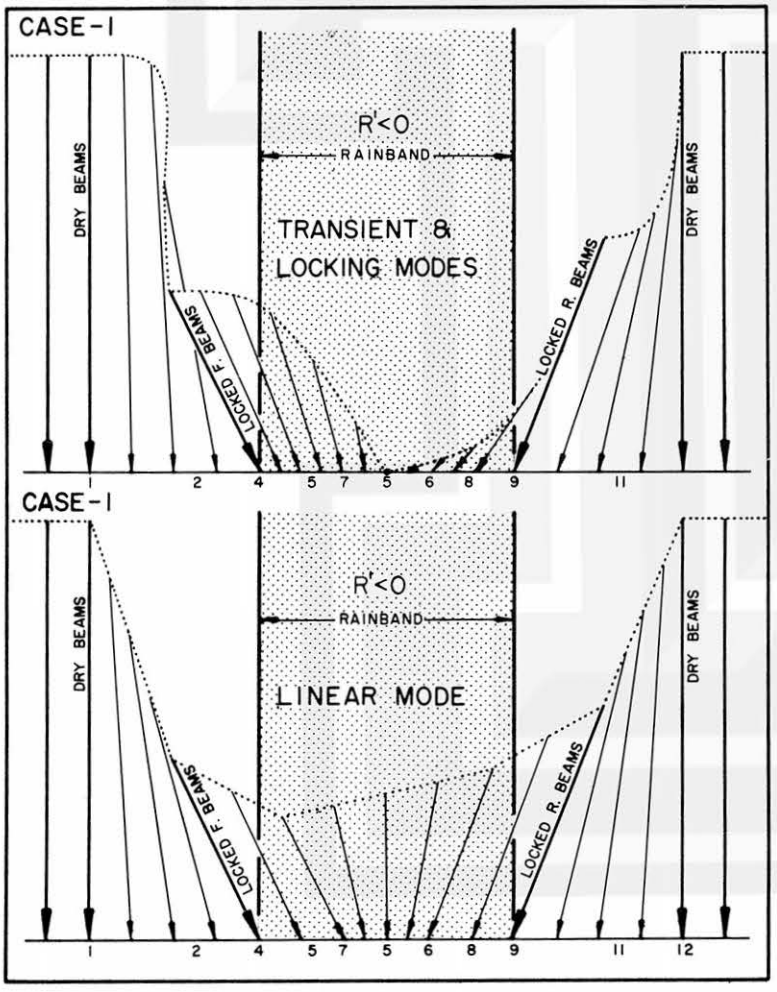

Fig. 12. Pattern of wet-beam winds corresponding to Case I in Fig. 11. The upper diagram represents the winds measured in non-linear modes and the lower, those measured in linear mode. Identical wetness was used for both diagrams. Note that the winds measured under the two locked beams, either front or rear, are unique in that they are independent of the tracking modes.

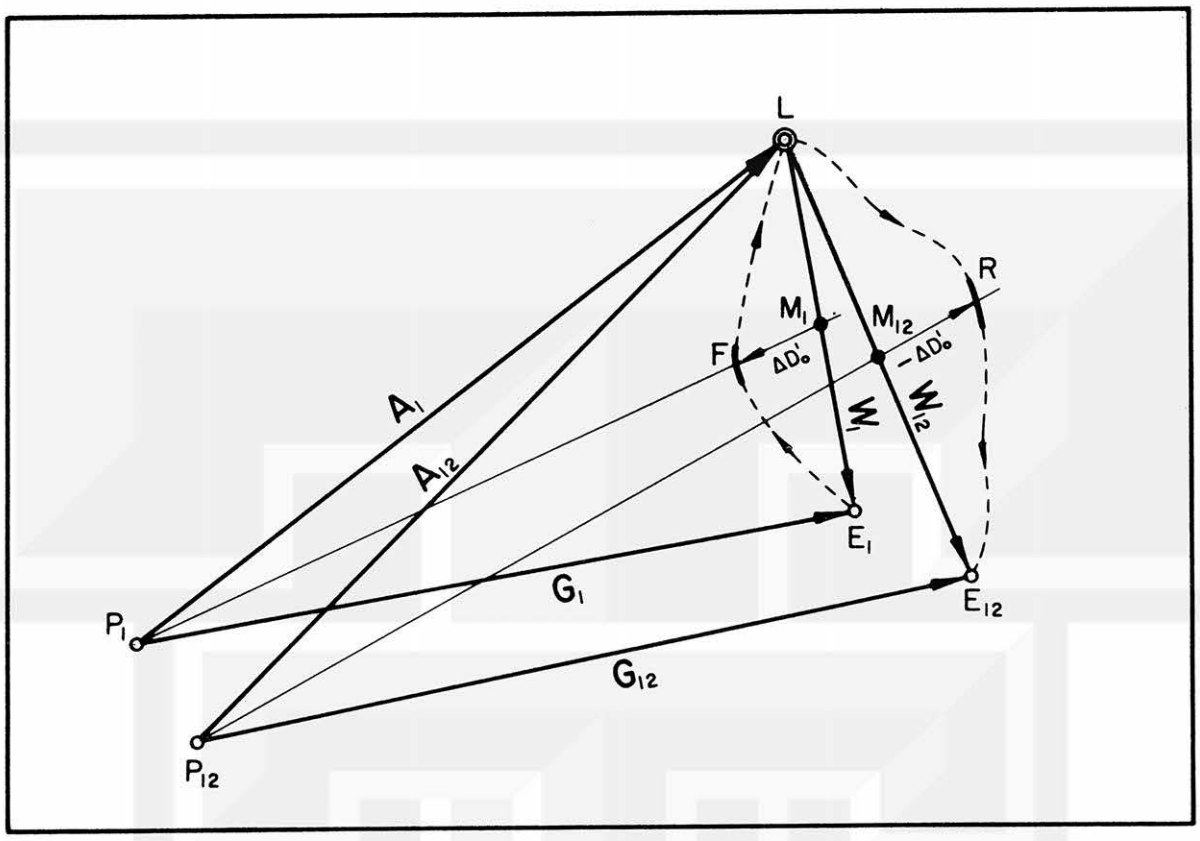

Fig. 13. Graphical determination of $\Delta D_o'$, which is proportional to the vertical velocity of the raindrops. The suffix, 1, denotes the beginning of the wet-beam winds and 12, their end. The measurements of $\Delta D_o'$ are always made on the line connecting P with M, the midpoint on the wind vector.

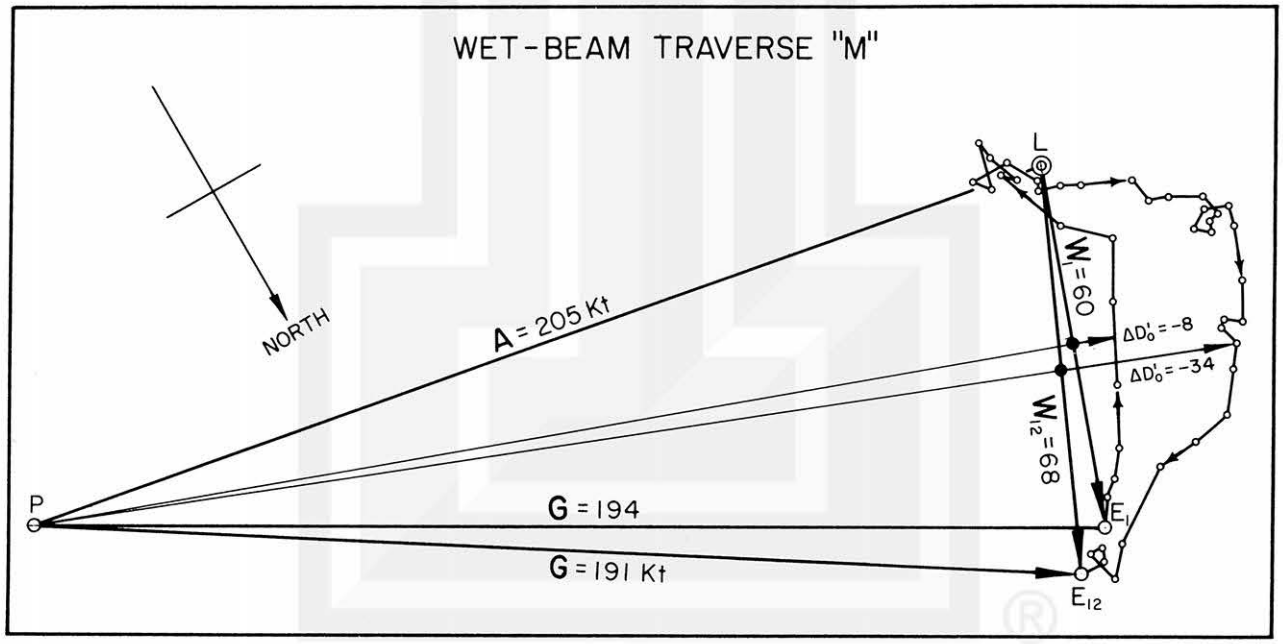

Fig. 14. Computation of the vertical velocity of the raindrops. Other aspects of the traverse, "M", appear in Figs. 2 and 4.

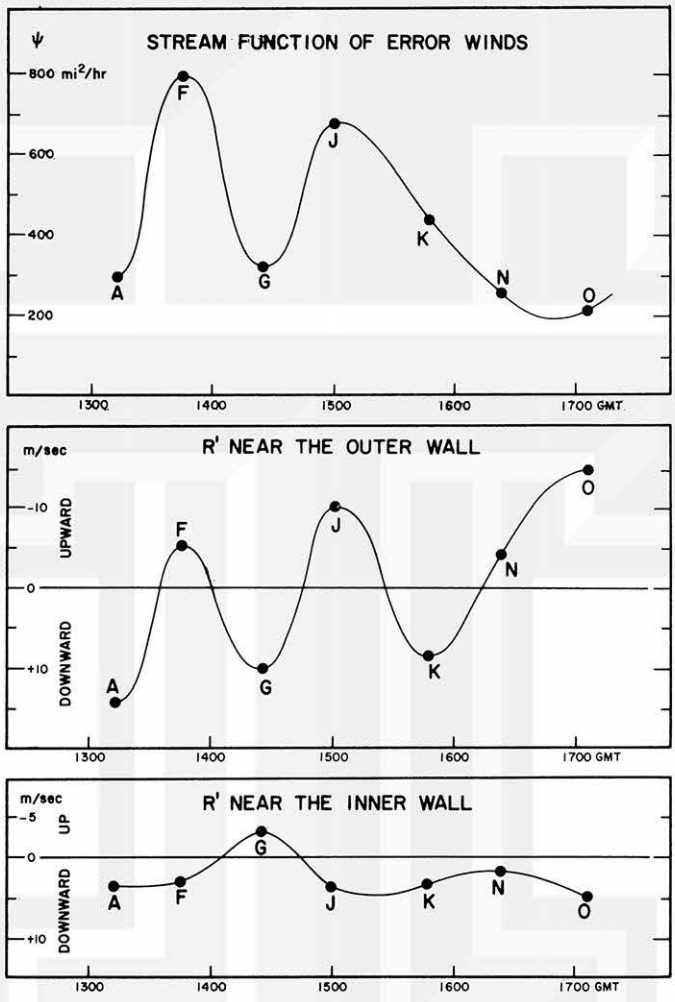

Fig. 15. Variation in the stream function of the error winds (upper), in the vertical velocity of the raindrops near the outer wall of the eye-wall rainband (middle), and in the vertical velocity of the raindrops near the inner wall of the eye-wall rainband (lower). Note that the variation in the vertical velocity is appreciable near the outer wall but remains rather constant near the inner wall.

MESOMETEOROLOGY PROJECT - - - RESEARCH PAPERS

(Continued from front cover)

42. A Study of Factors Contributing to Dissipation of Energy in a Developing Cumulonimbus - Rodger A. Brown and Tetsuya Fujita

43. A Program for Computer Gridding of Satellite Photographs for Mesoscale Research - William D. Bonner

44. Comparison of Grassland Surface Temperatures Measured by TIROS VII and Airborne Radiometers under Clear Sky and Cirriform Cloud Conditions - Ronald M. Reap

45. Death Valley Temperature Analysis Utilizing Nimbus I Infrared Data and Ground-Based Measurements - Ronald M. Reap and Tetsuya Fujita

46. On the "Thunderstorm-High Controversy" - Rodger A. Brown

47. Application of Precise Fujita Method on Nimbus I Photo Gridding - Lt. Cmd. Ruben Nasta

48. A Proposed Method of Estimating Cloud-top Temperature, Cloud Cover, and Emissivity and Whiteness of Clouds from Short- and Long-wave Radiation Data Obtained by TIROS Scanning Radiometers - T. Fujita and H. Grandoso

49. Aerial Survey of the Palm Sunday Tornadoes of April 11, 1965 - Tetsuya Fujita

50. Early Stage of Tornado Development as Revealed by Satellite Photographs - Tetsuya Fujita

51. Features and Motions of Radar Echoes on Palm Sunday, 1965 - Dorothy L. Bradbury and Tetsuya Fujita

52. Stability and Differential Advection Associated with Tornado Development - Tetsuya Fujita and Dorothy L. Bradbury

53. Estimated Wind Speeds of the Palm Sunday Tornadoes - Tetsuya Fujita

54. On the Determination of Exchange Coefficients: Part II - Rotating and Non-rotating Convective Currents - Rodger A. Brown

55. Satellite Meteorological Study of Evaporation and Cloud Formation over the Western Pacific under the Influence of the Winter Monsoon - K. Tsuchiya and T. Fujita

56. A Proposed Mechanism of Snowstorm Mesojet over Japan under the Influence of the Winter Monsoon - T. Fujita and K. Tsuchiya

57. Some Effects of Lake Michigan upon Squall Lines and Summertime Convection - Walter A. Lyons

58. Angular Dependence of Reflection from Stratiform Clouds as Measured by TIROS IV Scanning Radiometers - A. Rabbe